AUTOIMMUNITY

Joint profiling of gene expression and chromatin accessibility in pancreatic lymph nodes and spleens in human type 1 diabetes

Maryam Abedi[1,2,3,4,5]†, Priyadarshini Rai[1,2,3,4,5]†, Yeqiao Zhou[2,3,5,6]†, Chengyang Liu[2,4,5,7], Isabelle Johnson[1,2,3,4,5], Aditi Chandra[1,2,3,4,5], Maria Fasolino[1,2,3,4,5], Susan Rostami[2,4,5,7], Wei Wang[2,4,5,7], Zaw Min[2,4,5,7], Yanjing Li[2,4,5,7], Ming Yu[2,4,5,7], Atishay Jay[1,2,3,4,5], Vung Lian[2,8], Michael Silverman[2,8,9,10], Klaus H. Kaestner[1,3,4,5], Ali Naji[2,4,5,7], Robert B. Faryabi[2,3,5,6]*, Golnaz Vahedi[1,2,3,4,5]*

Type 1 diabetes (T1D) is an autoimmune disease characterized by the destruction of insulin-producing β cells in the pancreas. While current therapies focus on managing the disease, a deeper understanding of the underlying molecular mechanisms is crucial for developing disease-modifying interventions. In this study, we conducted a comprehensive analysis of gene expression and chromatin accessibility in nearly 1 million immune cells from the pancreatic lymph nodes and spleens of 43 individuals with and without T1D. We found a distinct subset of CD4 T cells specifically present in the pancreatic lymph nodes of organ donors representing the active disease stage. These cells exhibited elevated activity of *NFKB1* and *BACH2*, along with extensive chromatin remodeling associated with these transcription factors, which we also corroborated in a mouse model of T1D. A better understanding of these *NFKB1-BACH2*–expressing CD4 T cells may lead to therapeutic avenues for preventing or delaying T1D onset.

INTRODUCTION

Type 1 diabetes (T1D) is an autoimmune disease in which T lymphocytes target and destroy insulin-producing β cells in the pancreatic islets. Insulin, a hormone secreted by β cells, enables glucose uptake by peripheral tissues. For over a century, insulin replacement has been the only therapy for individuals with T1D (*1*). Nonetheless, the therapeutic landscape to delay or prevent T1D is rapidly changing as multiple ongoing clinical trials are examining immunotherapeutic approaches targeting cytokines and chemokines or selectively controlling specific immune cell types (*1*–*4*). Despite the promise of immunotherapy for favorable clinical outcomes in T1D, the precise immune events during the progression of autoimmunity remain to be elucidated.

We reasoned that molecular profiling of immune cells in pancreas-proximal immune organs could reveal the identity of immune subsets during disease progression. This approach became feasible through the National Institute of Diabetes and Digestive and Kidney Diseases [of National Institutes of Health (NIH)]–supported Human Pancreas Analysis Program (HPAP) (*5*–*7*). We received pancreatic lymph nodes (PLNs) from 43 organ donors grouped as nondiabetic controls, not diagnosed as diabetic but islet autoantibody positive (AAb^+) donors, and clinically diagnosed T1D donors. We performed deep immune profiling on cells residing in the PLN, a critical site for the drainage of immune cells into the pancreas and priming of autoreactive T cells (*8*, *9*) and the spleen tissues. We used single-nucleus multiome profiling (*10*), which allowed us to measure chromatin accessibility and gene expression in the same cell across more than 1 million cells collected from organ donors. This large-scale single-nucleus profiling revealed a distinct CD4 memory T cell subset in the PLNs and spleens of individuals with active T1D. These cells exhibited high *NFKB1* and *BACH2* expression and chromatin remodeling associated with these transcription factors. A similar subset was also found in the PLNs of the mouse model of T1D. Together, our work defines a conserved transcriptional and epigenetic program of CD4 memory T cells associated with T1D across species.

RESULTS

Single-nucleus multiome profiling of pancreatic lymph nodes and spleens from individuals with T1D

We first profiled the PLNs procured by the HPAP team from 13 individuals with T1D, 8 AAb^+ individuals without a diabetes diagnosis, and 14 healthy donors (HDs) as controls (Fig. 1A). Clinical information related to donors used in our study is provided in data file S1 and the PANC-DB portal (*11*). When feasible, our surgical team collected PLN tissues from different anatomical sections, i.e., the head, body, and tail of the pancreas. Because the complete set of head, body, and tail compartments was not available in all donors (data file S1), we combined cells from different PLN compartments.

We conducted multimodal single-nucleus assay for transposase-accessible chromatin (snATAC)/single-nucleus RNA sequencing

[1]Department of Genetics, University of Pennsylvania Perelman School of Medicine, Philadelphia, PA 19104, USA. [2]Institute for Immunology and Immune Health, University of Pennsylvania Perelman School of Medicine, Philadelphia, PA 19104, USA. [3]Epigenetics Institute, University of Pennsylvania Perelman School of Medicine, Philadelphia, PA 19104, USA. [4]Institute for Diabetes, Obesity and Metabolism, University of Pennsylvania Perelman School of Medicine, Philadelphia, PA 19104, USA. [5]HPAP Consortium, Children's Hospital of Philadelphia, Philadelphia, PA 19104, USA. [6]Department of Pathology and Laboratory Medicine, University of Pennsylvania Perelman School of Medicine, Philadelphia, PA 19104, USA. [7]Department of Surgery, University of Pennsylvania Perelman School of Medicine, Philadelphia, PA 19104, USA. [8]Division of Infectious Diseases, Children's Hospital of Philadelphia, Philadelphia, PA 19104, USA. [9]Perelman School of Medicine, University of Pennsylvania, Philadelphia, PA 19104, USA. [10]Department of Microbiology, Perelman School of Medicine, University of Pennsylvania, Philadelphia, PA 19104, USA.
†These authors contributed equally to this work.
*Corresponding author. Email: faryabi@pennmedicine.upenn.edu (R.B.F.); vahedi@pennmedicine.upenn.edu (G.V.)

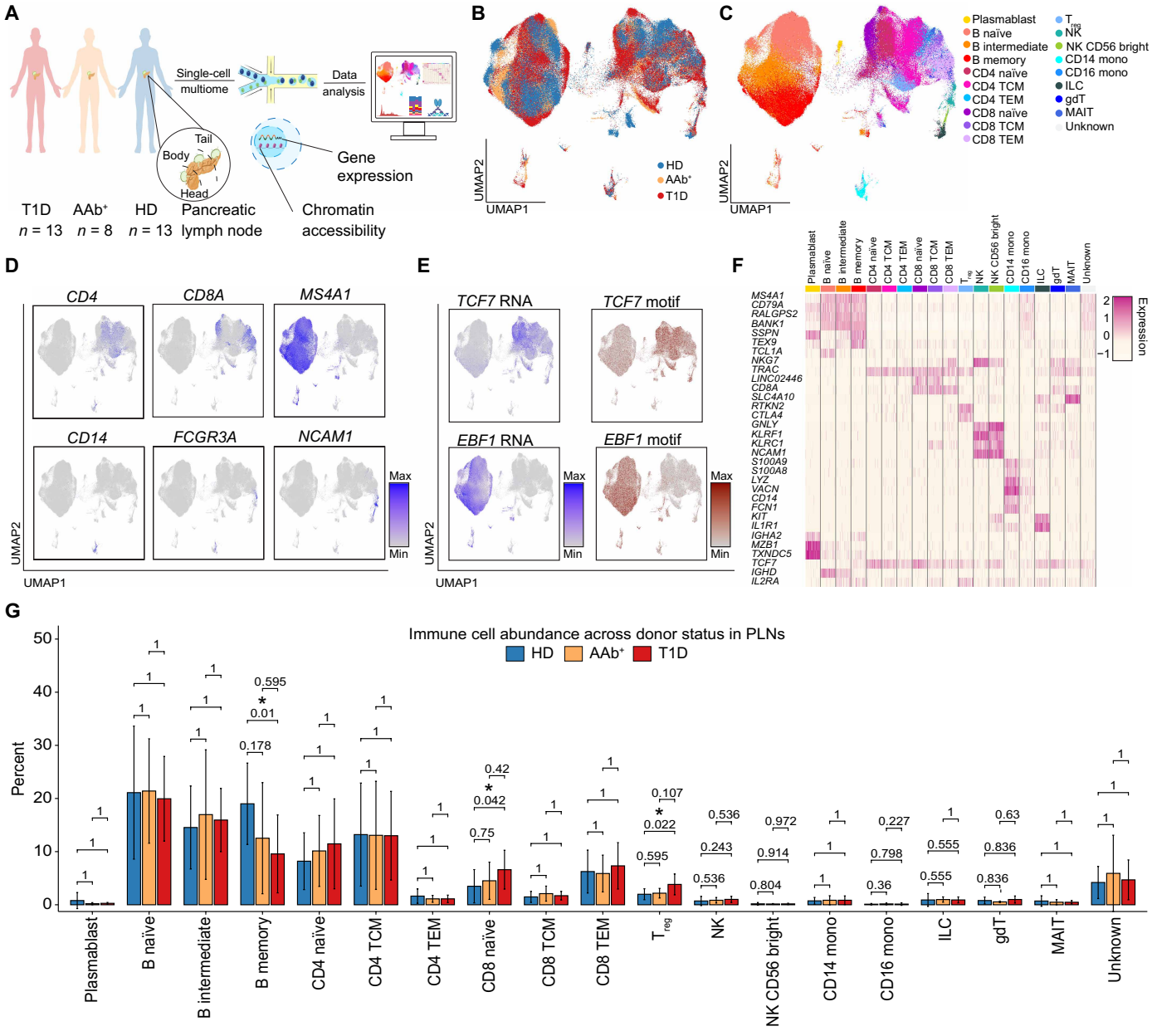

Fig. 1. Single-nucleus multiome profiling of pancreatic lymph node immune cells from organ donors with T1D. (**A**) Schematic outlining the experimental approach in this study for molecular profiling of immune cells in the PLN tissues. (**B** and **C**) UMAPs representing immune cells remained after quality control analysis labeled with donor status from 13 individuals with T1D, 8 islet autoantibody–positive (AAb^+) individuals without a diabetes diagnosis, and 14 HDs as controls (B), and immune cell annotation (C). (**D**) UMAPs representing RNA levels of cell-type–specific markers. (**E**) UMAPs representing RNA levels of B and T cell–specific transcription factors in addition to motif analysis in cCREs. (**F**) Heatmap showing the gene expression of cell markers used for immune cell annotation. (**G**) Bar chart showing immune cell abundance for cells pooled in different donor groups. Asterisks represent adjusted *P* value of ≤0.05 (Wilcoxon test). NK, natural killer; TCM, central memory T cells; TEM, effector memory T cells; ILC, innate lymphoid cells; gdT, gamma-delta T cells; MAIT, mucosal-associated invariant T cells.

(snRNA-seq) experiments in 565,887 cells obtained from 46+ PLN samples in 35 organ donors (fig. S1, A to C). The two modalities were integrated using weighted nearest neighbor (WNN) analysis (*10*). Uniform manifold approximation and projection (UMAP) was used on the WNN graph (fig. S1C), and clustering was performed using the RNA modality (fig. S1D). We removed any potential doublets (fig. S1E) and further filtered cells that did not pass the quality control for snRNA and snATAC assays (fig. S1, F to H). After this stringent filtering, we retained 302,631 individual cells with high quality in both RNA and ATAC modalities and observed mixing of samples in the UMAP plot (Fig. 1B and fig. S1, I to K), suggesting limited batch effects. To assess potential batch effects quantitatively, we calculated two established metrics (*12*, *13*), the local inverse Simpson's index (LISI) and the average silhouette width (ASW). We observed strong donor mixing with minimal clustering driven by batch effects (LISI of 6.04 and ASW of −0.23). We then applied batch correction using Harmony (*12*) and

observed only modest changes in the metrics after batch correction (LISI of 8.67 and ASW of −0.16). These findings indicate that batch and donor effects were already minimal and not major contributors to the observed clustering. Because integration approaches correcting for batch effects can obscure genuine biological signals, particularly in cross-tissue or cross-donor comparisons (*14*), we opted not to perform explicit batch correction to preserve biologically meaningful variation across donors and tissues.

For cell-type annotation, we followed a unified strategy for reference assembly and transfer learning on the basis of the RNA modality, reporting 30 distinct immune cell types (data file S2) (*15*). We further labeled 4.35% of cells as "unknown" considering the low confidence of cell annotation in these cells (Fig. 1C and fig. S1I). Visualizing the expression of marker genes across different annotated cell types on UMAP or heatmap, in addition to coverage plots of chromatin accessibility at cell-type–specific genomic loci, corroborated the high quality of our cell annotation (Fig. 1, D to F, and fig. S2A). Cells labeled as unknown as well as cell types represented by fewer than 100 cells were excluded from further analysis, resulting in 18 major cell types (fig. S2, B to D). We next identified similarities and differences for cell composition across individual donors (fig. S2E) and compared cell-type frequencies for cells grouped as T1D, AAb^+, and HD (Fig. 1G, fig. S2F, and data file S1). Our investigation did not yield substantial evidence indicating alterations in global cell composition in the PLN associated with T1D (Fig. 1G and fig. S2F).

We also determined the molecular landscape of $CD45^+$ immune cells in the spleens from the same donors, resulting in multiome data for 459,983 cells (Fig. 2A and fig. S3, A to C). We retained 328,855 individual cells with high-quality RNA and ATAC modalities (fig. S3, D to H). Dimensionality reduction with UMAP using spleen cells demonstrated mixing of cells across donors and disease groups (Fig. 2B and fig. S3, I and J). We followed a similar cell annotation strategy as described earlier and defined immune populations (Fig. 2C and fig. S3J). The expression of marker genes and coverage plots of chromatin accessibility at cell-type–specific genomic loci also confirmed the high quality of our cell annotation strategy in the spleens (Fig. 2, D to F, and fig. S4A). Cells labeled as unknown (1.19%) were excluded from further analysis, along with annotated cell types with fewer than 100 cells (fig. S4, B to D). Because of the larger number of cells available from the spleens, we were also able to perform the trimodal assay transcription, epitopes, and accessibility sequencing (TEA-seq) (*16*) on a subset of samples. In TEA-seq, determination of transcript abundance and chromatin accessibility is combined with selected proteomics to further refine cell-type annotation (*16*). Integration of cells from a subset of samples with TEA-seq confirmed our strategy for cell-type annotation (fig. S4, E to G). Overall, only moderate differences in cell composition were detected in the spleens of T1D donors (Fig. 2G; fig. S4, H and I; and data file S1). Thus, multidimensional data in PLNs and spleens provided us with the opportunity to define molecular signatures of T1D.

Large-scale changes in transcriptome of central memory CD4 T cells and memory B cells in T1D

We then conducted pseudo-bulk differential gene expression analysis across the major annotated cell types to compare donor groups. This analysis identified genes demonstrating increased or decreased expression in pairwise comparisons between donor groups. The largest differences in gene expression were observed between cells from T1D donors and HDs (Fig. 3, A and B, red and dark blue bars). The gene expression levels of cells from AAb^+ donors and HDs were also distinct. Nonetheless, comparison of T1D versus AAb^+ donors demonstrated a minimal number of differentially expressed genes for most cell types (Fig. 3A). Notably, comparison of various cell types highlighted central memory CD4 T cells to be the most distinct cell type between T1D donors and HDs in the PLN samples (Fig. 3A). The heatmap visualization of gene expression levels from central memory CD4 T cells by donor type corroborated their differential expression across donors (Fig. 3C). In the spleens, a greater number of genes were differentially expressed between donor groups compared with those in the PLNs. Monocytes and memory B cells exhibited the most pronounced changes in gene expression in the spleen T1D versus HD comparison (Fig. 3B). Notably, central memory CD4 T cells also showed a substantial number of differentially expressed genes in the spleens of T1D donors. Together, these findings highlight central memory CD4 T cells and memory B cells as key cell types with substantial gene expression alterations in T1D organ donors.

Next, we identified pathways enriched in differentially expressed genes, using gene set enrichment analysis (GSEA) (*17*). In the PLNs, genes associated with type I and type II interferon pathways in addition to the nuclear factor κB (NF-κB) signal transduction were selectively enriched among genes activated in central memory CD4 T cells of T1D compared with those of HD (Fig. 3, D and F), as well as among central memory CD4 T cells of AAb^+ versus HD donors (Fig. 3D). The interferon pathway has been implicated in many autoimmune diseases, including T1D (*18*, *19*). In the spleens, B cells and, to a lesser extent, CD4 T cells demonstrated enrichment of NF-κB pathways in T1D donors versus HDs (Fig. 3E). Expression levels of genes at the leading edge of the gene set representing the NF-κB pathway further confirmed their differential expression across donors in the PLN samples (Fig. 3G). Together, our analysis reports a strong activation of the interferon and NF-κB pathways in CD4 T cells of T1D and AAb^+ donors.

Large-scale chromatin remodeling in central memory CD4 T cells and memory B cells of T1D

Mapping chromatin accessibility using ATAC-seq at single-cell and bulk levels delineates candidate cis-regulatory elements (cCREs) and can be used to infer transcription factors that remodel the chromatin (*20*). From the 108,715 accessible chromatin regions identified in our ATAC modality, 80% overlapped ENCODE cCREs (*21*) and ~10% overlapped promoters (fig. S5, A and B). We then performed pseudo-bulk differential accessibility analysis between donor groups for each annotated cell type in the PLNs and the spleens, separately. We reported the number of cCREs whose accessibility increased or decreased in the pairwise comparisons between donor groups (Fig. 4, A and B). The largest number of differentially accessible cCREs was detected between T1D donors and HDs (Fig. 4, A and B). Although chromatin accessibly of cells from AAb^+ donors and HDs was also different, the T1D versus AAb^+ comparison demonstrated a minimal number of differentially accessible cCREs for any cell type (Fig. 4, A and B). In agreement with the gene expression analysis, central memory CD4 T cells of PLNs exhibited the most changes in chromatin accessibility between T1D donors and HDs (Fig. 4, A and C, and data file S3). In the spleens, memory B cells and $CD14^+$ monocytes displayed the largest difference in chromatin accessibility levels in the T1D versus HD comparison (Fig. 4B).

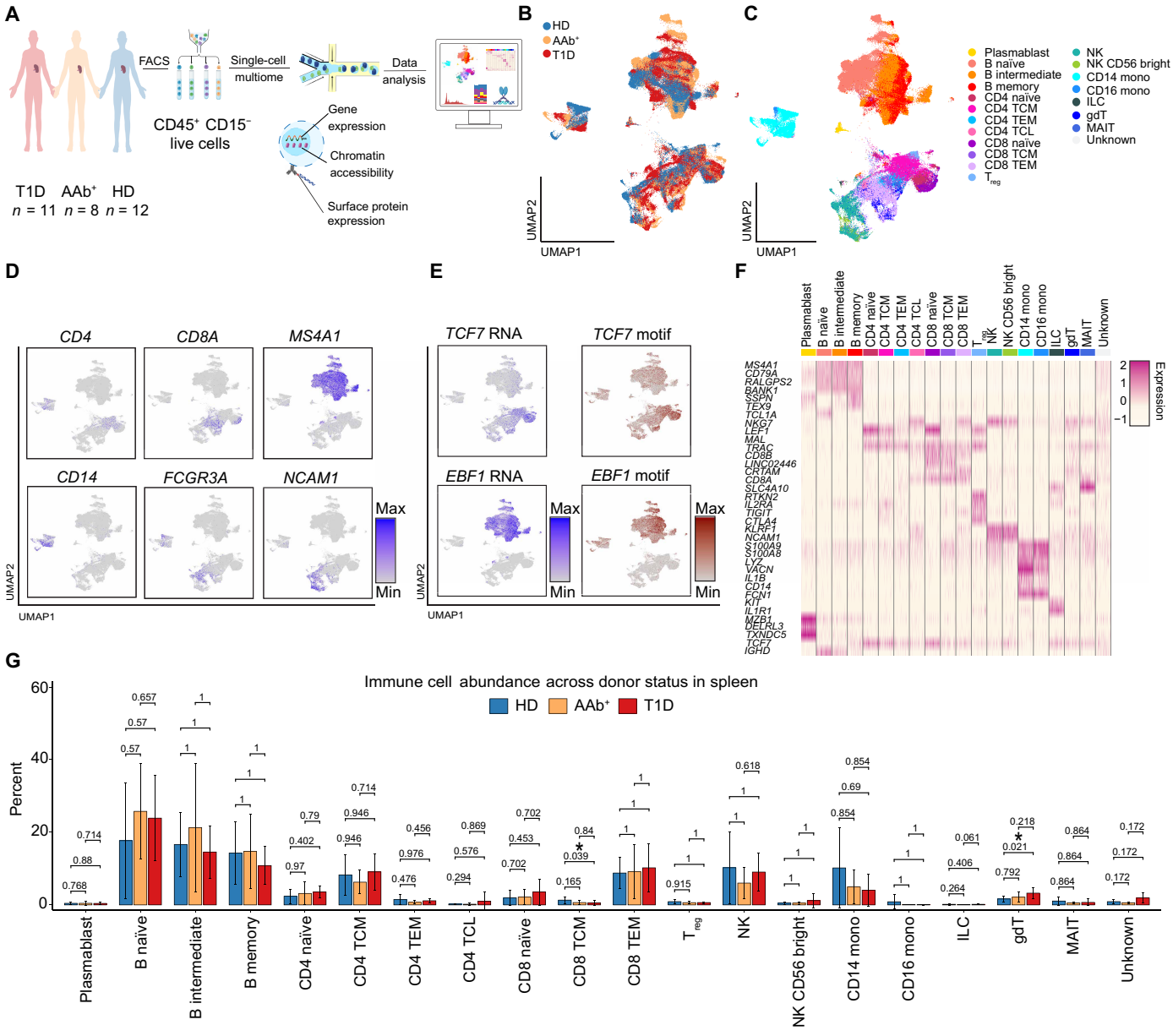

Fig. 2. Single-nucleus multiome profiling of splenic immune cells from organ donors with T1D. (**A**) Schematic outlining the experimental approach in this study for molecular profiling of immune cells in the spleen tissues. FACS, fluorescence-activated cell sorting. (**B** and **C**) UMAPs representing immune cells that remained after quality control analysis labeled with donor status from 13 individuals with T1D, 8 AAb$^+$ individuals without a diabetes diagnosis, and 14 HDs as controls (B), and immune cell annotation (C). (**D**) UMAPs representing RNA levels of cell-type–specific markers. (**E**) UMAPs representing RNA levels of B and T cell–specific transcription factors in addition to motif analysis in cCREs. (**F**) Heatmap showing the gene expression of cell markers used for immune cell annotation. (**G**) Bar chart showing immune cell abundance between donor status. Asterisks represent adjusted *P* value of ≤0.05 (Wilcoxon test).

To identify potential transcription factors involved in chromatin remodeling, we performed motif analysis within differentially accessible cCREs. We determined a strong enrichment of activator protein-1 (AP-1), in addition to NF-κB–p65, NF-κB–p50, and interferon-sensitive response element motifs, in cCREs selectively accessible in central memory CD4 T cells of T1D donors versus HDs (Fig. 4D). An even stronger enrichment of NF-κB–p65 along with AP-1 motifs was detected in cCREs selectively accessible in central memory CD4 T cells in AAb$^+$ donors versus HDs (Fig. 4D). The dimeric transcription factor complex AP-1 represents at least 15 proteins, including JUN, BACH2, ATF, MAF, or FOS (*22*). All AP-1 family transcription factors recognize the same core binding motif (TGASTCA, where S = C or G). Motif analysis tools arbitrarily assign a representative member (e.g., FOS) to this shared motif, and additional modalities such as gene expression can narrow down a specific family member. De novo motif analysis and seq-logo visualization of cCREs gained in T1D donors compared with HDs corroborated selective enrichment of NF-κB and AP-1 motifs in central

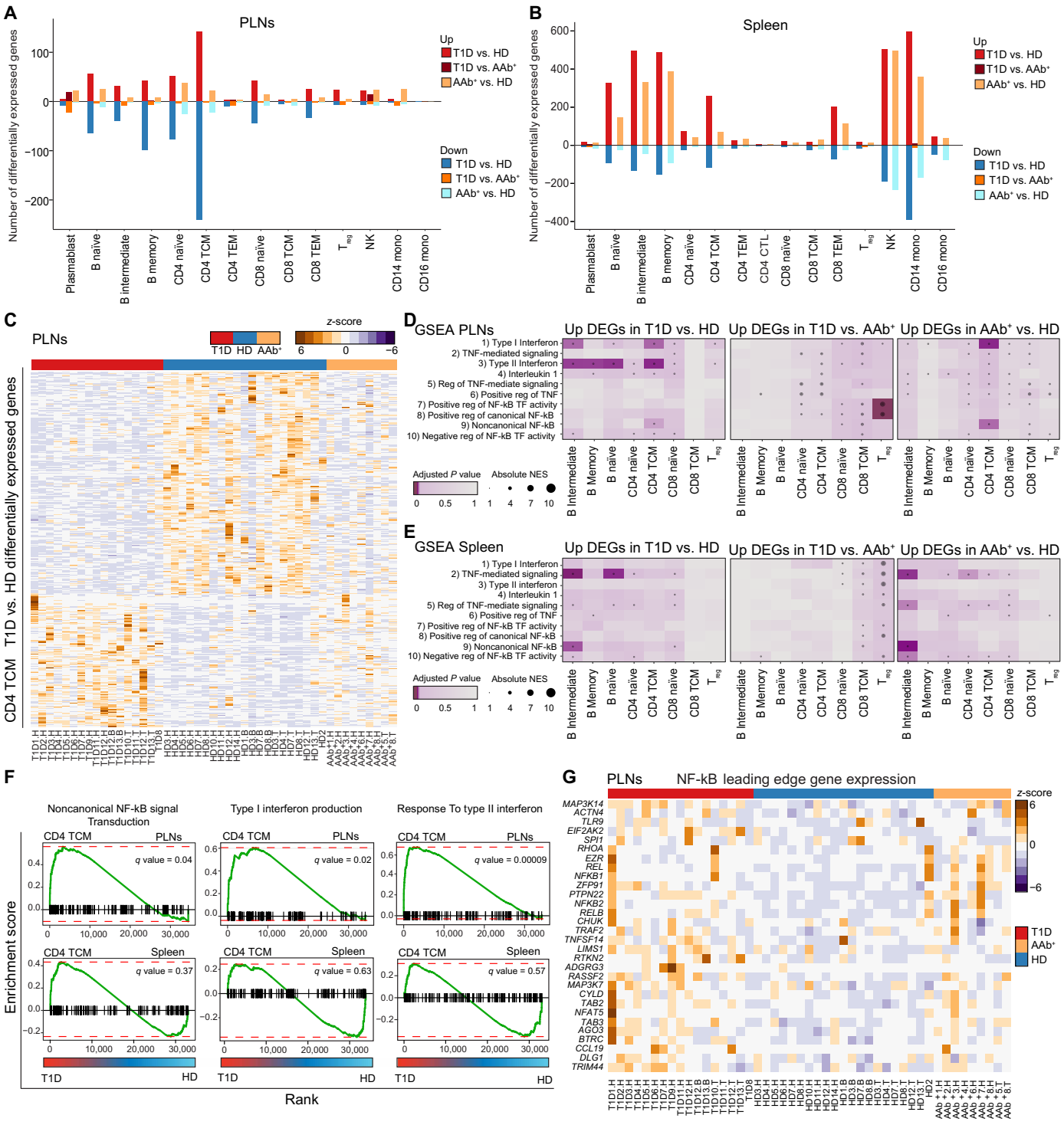

Fig. 3. Expression of genes associated with NF-κB and interferon pathways are elevated in central memory CD4 T cells in the PLNs of T1D. (**A** and **B**) Bar plots demonstrating the number of differentially expressed genes for pseudo-bulk analysis in each cell type between T1D versus HD, T1D versus AAb$^+$, and AAb$^+$ versus HD in PLNs (A) and spleens (B). (**C**) Heatmap representing the gene expression of differentially expressed genes between T1D and HD in central memory CD4 TCM in PLNs. (**D** and **E**) Preranked GSEA results in the PLNs (D) and the spleens (E). DEG, differentially expressed genes; NES, normalized enrichment score; TF, transcription factor. (**F**) GSEA plot depicting the enrichment of TNF, NF-κB, and interferon signaling in CD4 TCM of the PLNs, but not the spleens. (**G**) Heatmap showing the gene expression of the leading-edge genes for the NF-κB pathway extracted from GSEA output in PLNs.

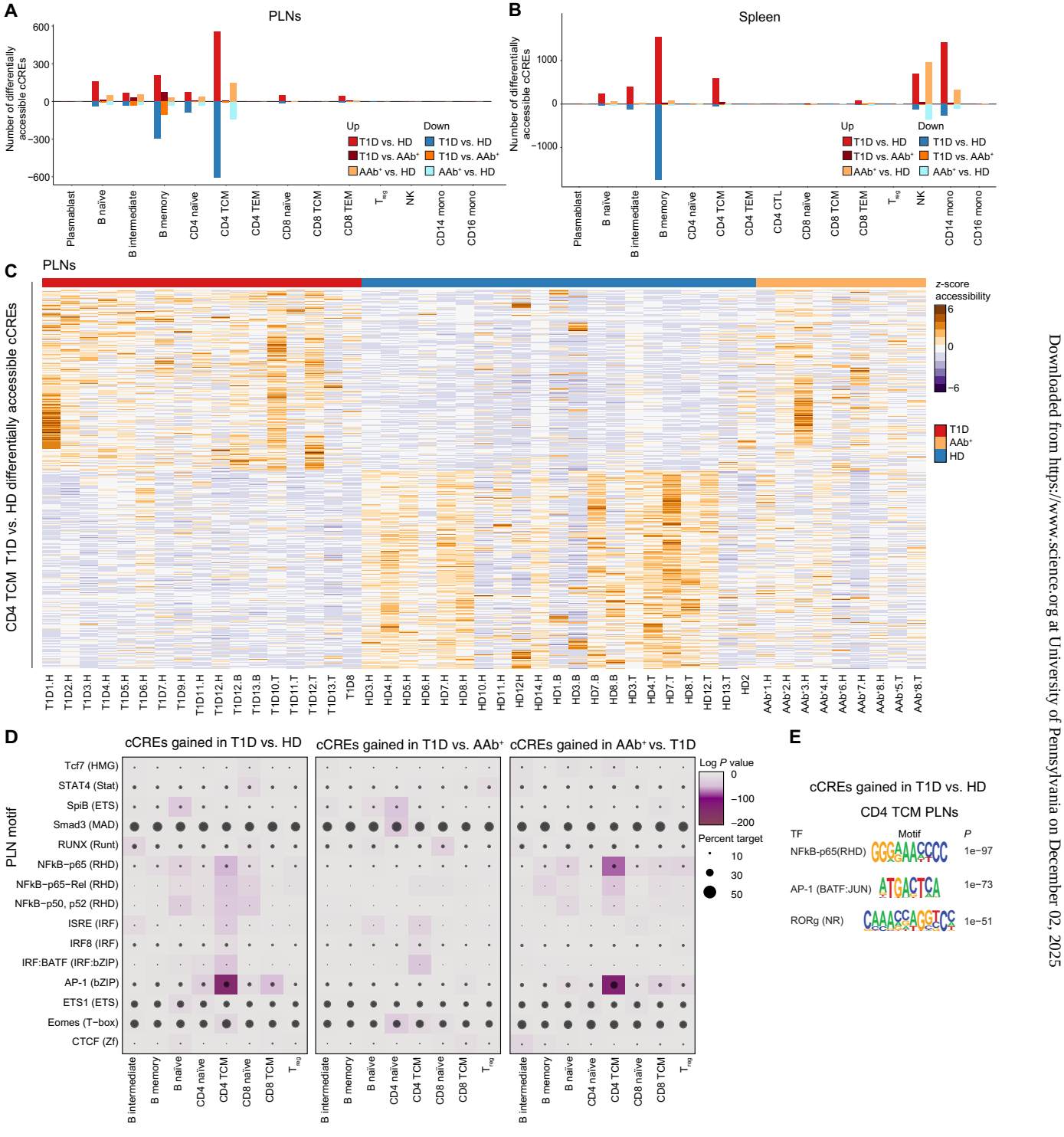

Fig. 4. Central memory CD4 T cells are the most epigenetically distinct immune cells in T1D PLNs. (**A** and **B**) Bar plots demonstrating the number of differentially accessible cCREs in each cell type between T1D versus HD, T1D versus AAb$^+$, and AAb$^+$ versus HD in the PLNs (A) and the spleens (B). (**C**) Heatmap representing chromatin accessibility levels for differentially accessible cCREs between T1D and HD in CD4 TCM in PLNs. (**D**) Motif analysis reveals top transcription factors enriched for each cell type for PLNs. (**E**) Seqlogo depicting de novo motif analysis using Homer in gained accessible chromatin regions in CD4 TCM of T1D donors compared with HDs in PLNs.

memory CD4 T cells residing in the PLNs (Fig. 4E). We did not detect an enrichment of AP-1 and NF-κB motifs in central memory CD4 T cells of the spleens (fig. S5, C and D). Instead, the naïve B cells in spleens of T1D and AAb^+ donors exhibited increased accessibility at cCREs with enrichment of NF-κB–p65, interferon regulatory factor–BATF, and SpiB (ETS) transcription factor binding sites (fig. S5D). These data suggest de novo chromatin remodeling of immune cells at different stages of T1D progression.

Association of T1D risk variants and chromatin accessibility in CD4 T cells

We next assessed the enrichment of T1D single-nucleotide polymorphisms (SNPs) within differentially accessible cCREs (fig. S6, A to H). We used a multiple regression model (*23*) and found that the strongest enrichment of T1D SNPs occurs within cCREs of central memory CD4 T cells whose accessibility increased in T1D donors compared with HD (fig. S6A and data file S4A). As described previously (*24*), we detected an enrichment of T1D-specific cCREs in SNPs associated with other immune-mediated diseases, such as rheumatoid arthritis (fig. S6A). We detected a strong enrichment of T1D SNPs within cCREs of regulatory T (T_{reg}) cells whose accessibility decreased in T1D donors compared with that in HDs, suggesting a link between genetics of T1D and loss of tolerance (fig. S6B and data file S4B). There was no significant enrichment of risk loci for diseases with limited immune contribution such as type 2 diabetes (T2D) and Alzheimer's disease in differentially accessible cCREs (fig. S6, C and D). Similar analysis in spleens suggested the enrichments of T1D SNPs within cCREs selectively accessible in $CD14^+$ monocytes, natural killer cells, and $CD8^+$ central memory T cells of T1D donors (fig. S6, E to H). Notably, we reported 56 genes whose proximal cCREs were differentially accessible in T1D and were proximal to T1D-associated SNPs (fig. S6I and data file S4A). Together, T1D-associated variants are enriched within cCREs that gained accessibility in immune cells of individuals with T1D.

NFKB1^{high}*BACH2*^{high} CD4 T cells are detected in the PLNs during active T1D

Upon closely examining the levels of gene expression and chromatin accessibility across CD4 T cells from each individual donor (i.e., Figs. 3, C and G, and 4C), we detected heterogeneity in aggregated levels of two modalities among donors, leading us to examine factors potentially contributing to this heterogeneity. In our cohort, the median age of T1D and AAb^+ donors was lower than that of HD (data file S1A), raising the question of whether age contributed to the molecular changes and heterogeneity detected among donors. Because of the unique and limited availability of organ donors, achieving precise age-matching across disease categories is challenging. To overcome this limitation, we performed single-nucleus experiments on eight additional donors: five T1D donors and three HDs (data file S1B). We processed these new samples using the same analytical strategy and retained 24,918 high-quality individual cells, increasing our total donor count to 43 (fig. S7, A to I). To create an age-matched cohort, we selected 24 donors, 8 from each disease group, with closely matched median ages (HD, ~24 years; AAb^+, ~21.5 years; and T1D, ~18 years) and comparable cell counts across donors (Fig. 5A and data file S1, C and D). Using the age-matched cohort, we reexamined signatures identified from our initial analysis. We conducted in-depth analyses on non-naïve CD4 T cells and non-naïve B cells in the age-matched cohort. After pooling cells annotated as central memory or regulatory CD4 T cells from PLNs and spleens, stratification of these cells revealed seven distinct CD4 T cell clusters among the donor groups (0 to 6) (Fig. 5, B and C, and fig. S7, J and K). Upon examination of T cell markers, we excluded cells in cluster 6, which expressed B cell markers (fig. S7J). T_{reg} cells grouped in cluster 1, expressing *CTLA4* and other canonical markers (fig. S7L).

We next asked whether CD4 T cells from specific disease groups formed distinct clusters. Whereas cells in clusters 0 and 1 showed comparable frequencies across disease groups (fig. S7K), cells in clusters 2 and 3 were restricted to T1D or AAb^+ individuals (Fig. 5D). Informed by our earlier analysis (Fig. 3G), we examined the expression of transcription factor *NFKB1* and found that it was moderately expressed in cells of all clusters (Fig. 5, D and E). However, the expression of *NFKB1* was markedly higher in cells grouped as clusters 2 and 3 compared with cells of other clusters (Fig. 5, D and E). Whereas clusters 0 and 1 contained cells uniformly distributed across all donors (Fig. 5F), cells in cluster 3 were exclusively derived from the PLNs of specific donors (Fig. 5G and data files S1E and S5). Notably, cells from T1D donor 1, an individual diagnosed with T1D at the time of admission without prior suspicion, contributed significantly to cluster 3 (Fig. 5G). Moreover, cells from the PLN of AAb^+ donor 3 expressing high GAD titers and AAb^+ donor 7 expressing three autoantibodies, GAD (glutamic acid decarboxylase), IA-2 (islet antigen-2), and ZnT-8 (zinc transporter 8), demonstrated transcriptome similarity to cells from the PLN of T1D donor 1 by aggregating in cluster 3. A smaller number of cells from other donors including AAb^+ donor 2 and T1D donor 2 grouped in cluster 3 as well (Fig. 5G and data file S1E). Conversely, cells aggregated in cluster 2 were exclusively from the spleens and predominantly came from T1D donor 2 in addition to donors with major contributions to cluster 3 (AAb^+ donor 3 and AAb^+ donor 7, T1D donor 1), AAb^+ donor 5, and T1D donor 10 (Fig. 5, C and G, and data file S1E). Given that T1D donor 1 was confirmed as having active T1D and that individuals with multiple autoantibodies or high antibody titers are at increased risk of developing T1D, we designated donors in cluster 3 as representing active T1D.

We also assessed whether excluding the most dominant donor from each cluster (cells from T1D donor 1 in cluster 3 and cells from T1D donor 2 in cluster 2) would affect our gene expression analysis. We identified differentially expressed genes in cells from all donors in each cluster or excluding the top donor relative to the shared reference cluster (cluster 0) and then evaluated the correlation of fold changes (log_2) between these differentially expressed genes lists. These comparisons revealed strong correlations in differences in gene expression values [coefficient of determination (R^2) = 0.94], supporting the conclusion that multiple donors contribute to the disease-specific clusters identified in our study (fig. S7M).

We next sought to determine whether the elevated *NFKB1* transcript levels were also reflected at the protein level in PLN tissues. Using limited fixed tissue samples collected by the HPAP team, we obtained PLN sections from the triple autoantibody–positive AAb^+ donor 7, representing active T1D, and a healthy control donor. Immunofluorescence (IF) staining was performed to assess the expression of CD4, CD45RO (a marker of memory T cells), and NFKB1 across the PLN sections (Fig. 5H). To quantitate the expression of three proteins in AAb^+ donor 7 compared with that in the healthy control, we followed a rigorous computational approach relying on cell segmentation and grouped cells into naïve and memory CD4 T cells based on the expression of CD4 and CD45RO in both donors.

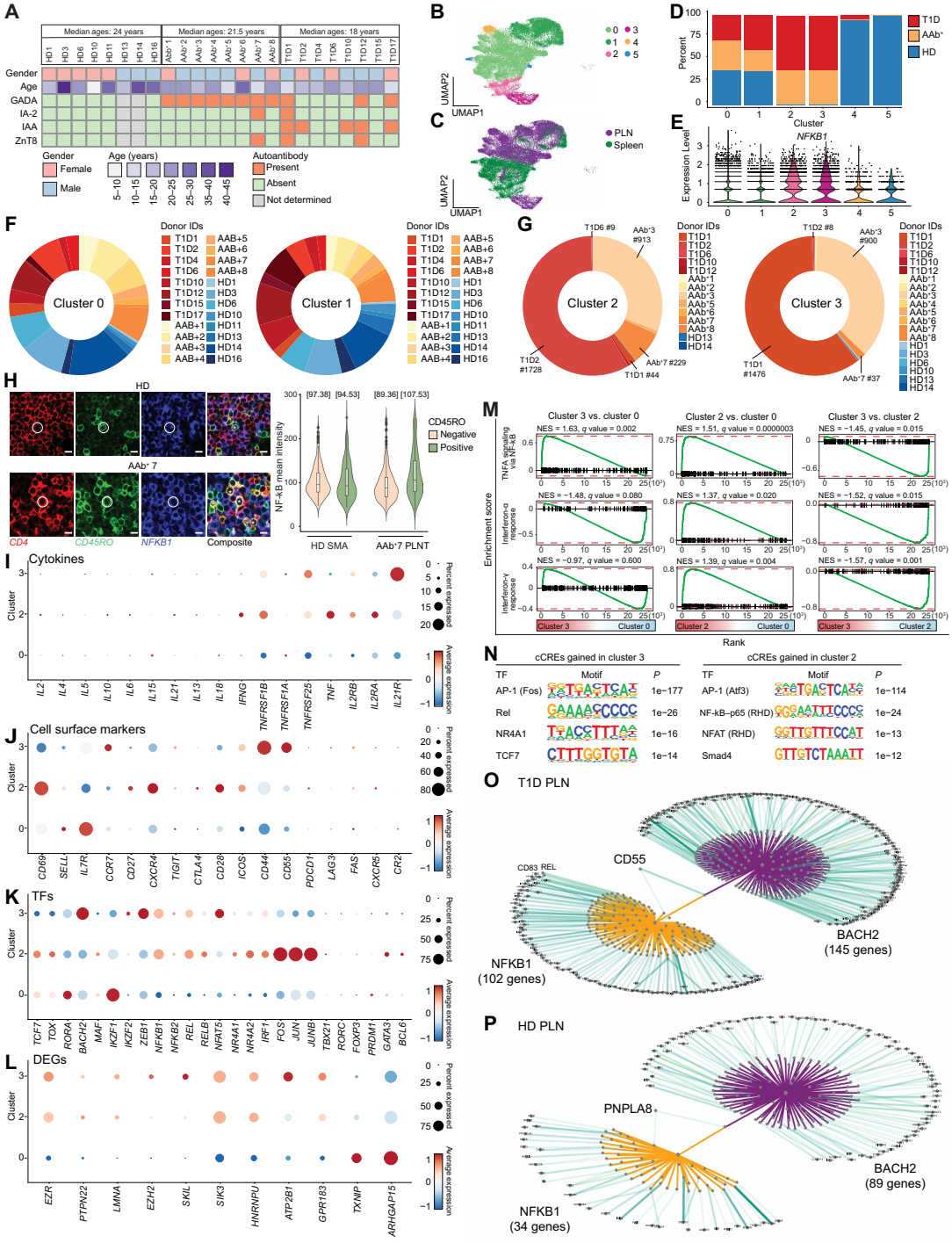

Fig. 5. *NFKB1*^{high}*BACH2*^{high} CD4 T cells are detected in the PLNs during active T1D. (**A**) Clinical and demographic information of the age-matched cohort. (**B** and **C**) UMAPs representing CD4 memory cells and T_{reg} cells after reclustering labeled with cluster number (B), and tissue of origin (C). (**D**) Stacked bar chart indicating the donor status composition in each cluster. (**E**) Violin plot shows *NFKB1* expression across clusters. (**F** and **G**) Circle plots depicting donor composition across nondisease clusters (F) and disease-associated clusters (G). (**H**) Immunostaining validation of NFKB1 expression in PLN sections from the triple autoantibody–positive AAb$^+$ donor 7, representing active T1D, and a healthy control donor (not used in single-cell profiling). Cells were grouped into naïve and memory CD4 T cells on the basis of the expression of CD4 and CD45RO in the donors, and the expression of NFKB1 protein across naïve and memory CD4 T cells was evaluated. Mean values are shown within brackets. PLNs near superior mesenteric artery on the pancreas are annotated as SMA. PLNT refers to lymph nodes located at the pancreas tail. (**I** to **L**) Dot plots showing the expression of cytokines (I), cell surface markers (J), transcription factors (K), and top differentially expressed genes in clusters 2 and 3 compared with those in cluster 0 (L). (**M**) Pre-ranked GSEA plots depicting pathway enrichment for clusters 3 and 2 versus cluster 0. (**N**) Seqlogo depicting de novo motif analysis using Homer in gained accessible chromatin regions in clusters 3 and 2 compared with those in cluster 0. (**O** and **P**) SCENIC+-derived network plots illustrating regulatory interactions between target regions and associated genes within NFKB1 and BACH2 eRegulons in PLNs of T1D (O) and HDs (P).

We evaluated the expression of NFKB1 protein across naïve and memory CD4 T cells in two representative images (Fig. 5H and fig. S7N). Given the age of these samples, collected over 8+ years, we expected some variation in data quality. To enable accurate comparisons, we applied quantile normalization to each protein staining dataset. Originally developed for microarray data analysis (*25*), quantile normalization corrects for systematic technical variation across samples while preserving relative differences within each sample. The HD PLN contained naïve and memory CD4 T cells with comparable levels of NFKB1 (Fig. 5H). In contrast, the mean NFKB1 protein level was higher in memory CD4 T cells compared with that in naïve CD4 T cells of AAb^+ donor 7 (Fig. 5H). These data confirmed elevated levels of NFKB1 protein in CD4 memory T cell populations in the donor expressing three autoantibodies representing active T1D.

We explored the identity of cells in T1D-associated clusters 2 and 3 and evaluated the expression of genes encoding transcription factors, cytokines, and cell surface markers (Fig. 5, I to L). In addition to *NFKB1* and *REL* associated with the NF-κB pathway, the AP-1 transcription factor *BACH2* was selectively expressed in cells comprising cluster 3 but not clusters 0 or 2 (Fig. 5K). *BACH2* expression in T cells has been implicated in repressing effector responses (*26*) and enforcing stem-like T cell identity upstream of TCF-1 (*27*). The AP-1 transcription factors *FOS*, *JUN*, and *JUNB*, but not *BACH2*, were highly expressed in cells of cluster 2 compared with those in cells in clusters 0 or 3 (Fig. 5K). Cells in clusters 2 and 3, in addition to cluster 0, expressed very low level of cytokines and moderate levels of *TCF7*, corroborating that cells in these clusters are not effector cells (Fig. 5, I and K). Transcription factors *NFAT5* and *NR4A1* downstream of T cell receptor signaling were expressed in clusters 3 and 2, respectively (Fig. 5K). Cells in cluster 3 expressed memory markers like *CD44* and *CCR7* in addition to *TNFRSF25*, also known as DR3, the receptor of the tumor necrosis factor (TNF) family cytokine TL1A (Fig. 5, I and J). Cells in cluster 2 had moderate expression of *BCL6*, the master regulator of T follicular helper cells, although these cells did not express *IL21*. We also performed differential gene expression analysis between clusters 3 and 0, which represented CD4 T cells from all donor groups (Fig. 5K). A unique set of genes was highly expressed in cells of cluster 3 including *GPR183*, also known as *EBI2*, which has a major role in immune cell trafficking (*28*), in addition to *SIK3*, *EZR*, *HNRNPC*, and *SKIL*. Genes associated with TNF signaling via NF-κB were also overexpressed in clusters 2 and 3 (Fig. 5M). Moreover, interferon-related genes were strongly up-regulated in cluster 2 cells from the spleens and cluster 0 cells from the PLNs, but not in cluster 3 cells from the PLNs (Fig. 5M). The enrichment of these pathways was stronger in cells of cluster 2 versus cluster 3 (Fig. 5M). Together, our analysis revealed transcriptional signatures of the T1D-associated CD4 T cell subpopulation.

NFKB1^{high}*BACH2*^{high} CD4 T cells have distinct chromatin signatures in the PLNs during active T1D

We next assessed whether chromatin accessibility measurements corroborate changes in gene expression in T1D-associated clusters 2 and 3. To identify transcription factors affecting chromatin accessibility during active T1D, we performed de novo motif analysis and detected strong enrichments for AP-1, NF-κB–p65, Rel, Nr4a1, Nfat, and Tcf7 motifs in cCREs selectively more accessible in T1D-associated clusters 2 and 3 in comparison with cluster 0 (Fig. 5N). Notably, the most substantial motif within cCREs of clusters 3 and 2 belonged to the AP-1 family. Because BACH2—but not other AP-1 proteins such as FOS, JUN, or JUNB—is expressed in cluster 3 (Fig. 5K), we inferred that the AP-1 motif enrichment in cluster 3 cCREs likely reflects BACH2 activity rather than that of other AP-1 family members. Hence, the elevated expression of *BACH2*, *NFBK1*, *NR4A1*, *NFAT*, and *TCF7* from the cognate protein families corroborates the footprint of these transcription factors on the open chromatin of cells in cluster 3 (Fig. 5N).

We next assessed the significance of the *NFKB1* and *BACH2* transcription factors in T1D cells independent of clustering-based approaches. We inferred the enhancer-driven gene regulatory networks or "eRegulons" using SCENIC+ (Fig. 5, O and P, and fig. S8) (*29*). This method identifies candidate enhancers from ATAC-seq, defines enriched transcription factor-binding motifs, and links transcription factors to candidate enhancers and target genes using ATAC-seq and RNA-seq measurements. SCENIC+ allowed us to fully exploit the simultaneous profiling of gene expression and chromatin accessibility and inferred targets of *NFKB1* and *BACH2* (Fig. 5, O and P, and fig. S8). In line with our separate analysis of gene expression and chromatin accessibility, both *NFKB1* and *BACH2* had larger eRegulons in T1D cells versus HD cells (*NFKB1*: 102 target genes and 143 target regions in T1D versus 34 target genes and 48 target regions in HD; *BACH2*: 145 target genes and 223 target regions in T1D versus 89 target genes and 118 target regions in HD) (Fig. 5, O and P, and fig. S8). Notably, two cCRE targets of BACH2 at *CCR7* and *FLI1* loci overlapped with SNPs (rs607703 and rs112401631) disrupting transcription factor binding sites (fig. S8, G and H). Thus, a strategy using both modalities independent of clustering strategies also indicates the importance of elevated *NFKB1* and *BACH2* in T1D lymphocytes.

T1D-associated B cells in the spleens show interferon-responsive signatures

Extending our in-depth analysis to non-naïve B cells in the PLNs and the spleens of our age-matched cohort led to grouping of B cells into nine clusters (0 to 8) (Fig. 6, A and B, and fig. S9A). Although clusters 0, 1, 2, 4, 5, and 8 were represented by cells from the three disease groups, cells grouped as clusters 3, 6, and 7 did not belong to any HDs (Fig. 6C). The expression of *NFKB1* was the highest in B cells grouped in clusters 6 and 7 compared with that in other clusters (Fig. 6, C and D). Unlike T cells, disease-specific B cells were exclusive to the spleens (Fig. 6, B and C). Clusters 0, 1, and 2 comprise cells from all donors across three disease groups (Fig. 6, E to G), whereas most of B cells from T1D and AAb^+ donors contributed to disease-associated clusters 3 and 6 (Fig. 6, H to J). Cluster 3 contained cells from AAb^+ donor 6, T1D donor 1, T1D donor 6, T1D donor 2, AAb^+ donor 5, and T1D donor 12, whereas cluster 6 contained cells from AAb^+ donor 3, AAb^+ donor 7, and T1D donor 10 (Fig. 6, H and I, and data file S1F). Cells in cluster 7 predominantly came from T1D donor 2 in addition to moderate contributions from donors AAb^+ donor 6, AAb^+ donor 7, and T1D donor 1 (Fig. 6J and data file S1F). We also reported that the transcriptome landscape of disease-specific B cell clusters 3 and 6 was not dependent on the most dominant donor (fig. S9B). Together, B cells in the spleens of AAb^+ and T1D donors demonstrated distinct gene expression signatures.

We evaluated the expression of cytokines, transcription factors, and cell surface markers and obtained the top differentially

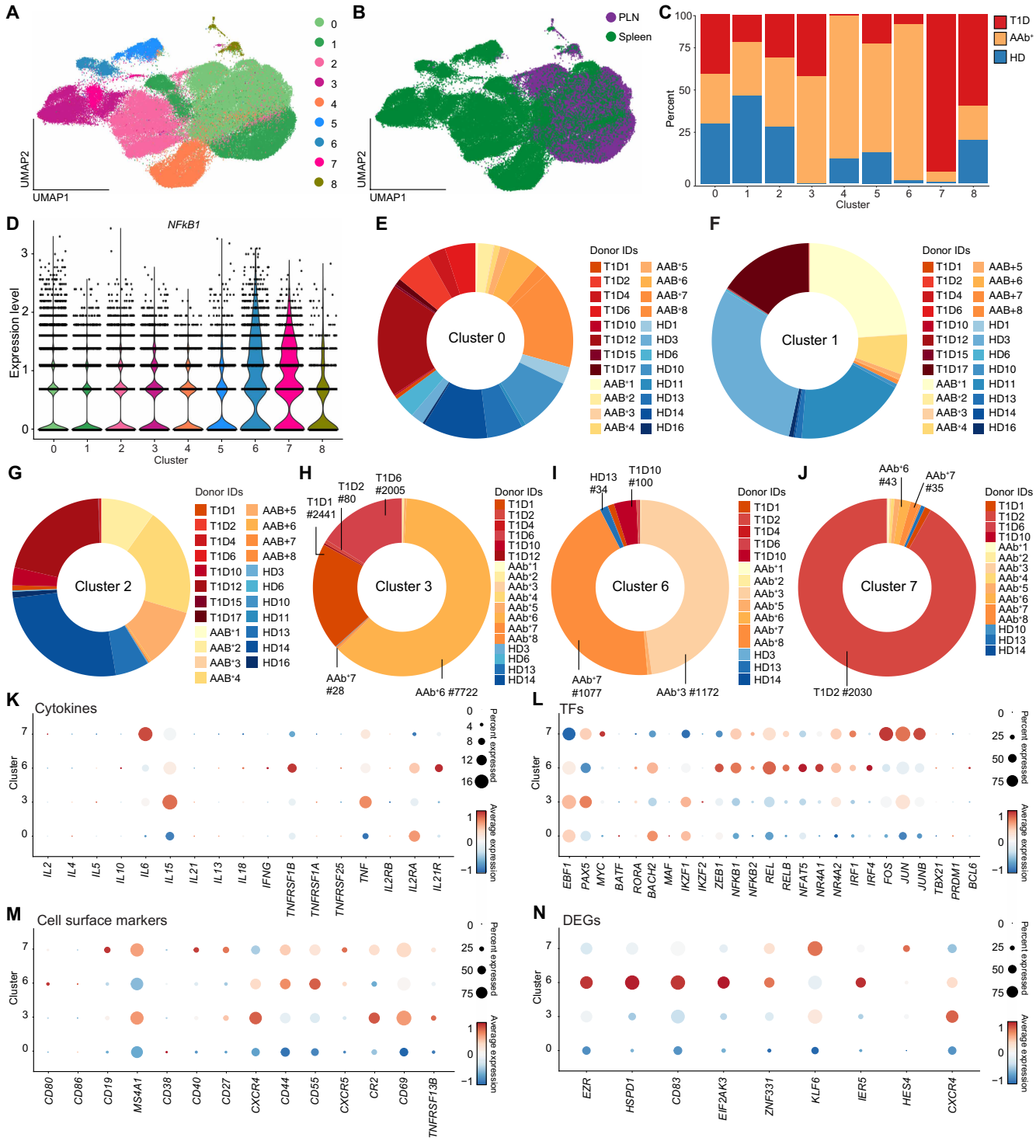

Fig. 6. T1D-associated splenic B cells show interferon-responsive signatures. (**A** and **B**) UMAP representing nonnaïve B cells after reclustering labeled with the cluster numbers (A), and tissue of origin (B). (**C**) Stacked bar chart indicating the donor status composition in each cluster. (**D**) Violin plot shows NF-κB expression across clusters. (**E** to **J**) Circle plots depicting donor composition across nondisease clusters [(E) and (F)] and disease-associated clusters [(G) to (J)]. (**K** to **N**) Dot plots showing the expression of cytokines (K), transcription factors (L), cell surface markers (M), and top differentially expressed genes in clusters 3, 6, and 7 compared with cluster 0 (N).

expressed genes between clusters 3, 6, and 7 compared with those in cluster 0 (Fig. 6, K to N). The master regulator of germinal center B cells, *BCL6*, was not expressed in any of these clusters (Fig. 6L). Both *CD27* and *TNFRSF13B* were moderately expressed in cells grouped in clusters 3 and 7, suggesting their annotation as memory B cells (Fig. 6M). Elevated activity of TNF signaling pathway via NF-κB, as well as interferon-γ responses, was detected in T1D-associated B cell clusters (fig. S9C). These observations were confirmed with motif analysis on differential accessible cCREs, which revealed the enrichment of NF-κB–related transcription factors like *REL* and interferon-related TFs like *IRF4*, and *EGR1* in the T1D-associated clusters (fig. S9D). Thus, B cells in the spleens of most AAb^+ and T1D donors differ markedly from those of HDs, showing elevated interferon-γ and NF-κB signatures.

NFKB1^{high}*BACH2*^{high} CD4 T cells are detected during presymptomatic stages in NOD mice

We examined whether T1D signatures of human CD4 T cells were generalizable to the nonobese diabetic (NOD) mouse strain. Female NOD mice develop diabetes at a rate of ~80% by 30 weeks of age, whereas males exhibit a significantly lower incidence. We performed snATAC/snRNA multiome experiments on $CD45^+$ immune cells purified from the PLNs of a 9-week-old female NOD mouse (Fig. 7A). We also performed multiome experiments on $CD45^+$ cells purified from the PLNs of a 19-week-old female with recent onset of diabetes established by glucosuria (Fig. 7, A to D). As a control, we analyzed age- and sex-matched Eα16/NOD littermates, which are genetically identical to the NOD strain except for a targeted modification that enables the expression of the major histocompatibility complex (MHC) class II Eα transcript, conferring protection against T1D (*30*–*33*). We measured gene expression and chromatin accessibility in $CD45^+$ cells purified from the PLNs of four mice described above. Following our standard computational workflow, we detected 44,453 cells across all mice, and after filtering doublets and low-quality cells, we focused our analysis on 38,414 immune cells (fig. S10, A to C). We applied a similar clustering approach described earlier and detected 22 clusters (Fig. 7, E to G). On the basis of the expression of marker genes, we annotated clusters as naïve, effector, and memory T and B cells in addition to T_{reg} cells (Fig. 7F and fig. S10C).

We first assessed the expression of the *Nfkb1* transcription factor across all clusters in mice. CD4 T cells in cluster 14 expressing the memory marker *Ccr7* had the highest level of *Nfkb1* (Fig. 7H and fig. S10C). Cells in this cluster did not come from any specific mouse (fig. S10D). The expression of genes encoding cytokines, transcription factors, and cell surface markers confirmed cell annotation in cluster 14 (Fig. 7, J to M). Similar to cluster 3 in human PLNs, CD4 T cells in cluster 14 expressed low levels of cytokine genes but high levels of *Bach2* and *Nfkb1* transcription factors (Fig. 7, J to M). Genes differentially expressed in cluster 14 compared with all other CD4 T cells from mouse PLNs, such as *Gpr183*, *Ezr*, and *Hnrnpc*, were highly expressed in active T1D cluster 3 in the human PLNs (Figs. 5K and 7M). Notably, the top 200 up-regulated genes in cells forming cluster 3 in human PLNs, such as *NFKB1*, *BACH2*, *SIK3*, and *GPR183*, were enriched among genes up-regulated in cells forming cluster 14 in NOD mice (Fig. 7I). These 200 genes were also up-regulated in cells of cluster 14 coming from 9-week-old NOD mouse in comparison with cells from 9-week-old Eα16 mouse (Fig. 7I). The comparison of cells from 19-week-old NOD versus 19-week-old Eα16 animals grouped in cluster 14 did not show this enrichment (Fig. 7I). We also compared differentially expressed genes associated with mouse cluster 14 and human cluster 3 each in comparison with the reference nondisease clusters, resulting in 107 common genes between active T1D clusters in humans and mice (Fig. 7N and data file S6; Fisher's exact test, odds ratio of 7.73, $P < 2.2 \times 10^{-16}$).

Using chromatin accessibility measurements, we examined transcription factors whose recognition sites were selectively enriched within cCREs specific to cluster 14. We found recognition sites for NF-κB–p65, AP-1, Nr4a1, and Tcf7 motifs confirming the potential influence of *Nfkb1*, *Nr4a1*, and *Tcf-1* on chromatin remodeling of cells in cluster 14 during active T1D (Figs. 5M and 7O). Similar to human PLNs, because *Bach2* was highly expressed in cluster 14, we inferred that the AP-1 motif enrichment in cluster 14 cCREs likely reflects BACH2 activity. We also found 169 common gained cCREs among orthologous cCREs between cluster 14 in mice and cluster 3 in humans (Fig. 7P; Fisher's exact test, odds ratio of 5.04, $P < 2.2 \times 10^{-16}$). Motif analysis on cCREs shared between active T1D clusters in humans and mice resulted in the enrichment of AP-1, Tcf7, Nr4a1, and Nfkb1 (Fig. 7Q). In sum, an *Nfkb1*^{high}*Bach2*^{high} CD4 T cell state marked by gene expression and epigenetic similarities in the human and mouse PLNs are associated with active T1D.

Gene signatures of T1D detected in the spleens can be detected in circulation

We next aimed to examine whether the active T1D signatures that we identified in T and B lymphocytes of organ donors could be detected in peripheral blood mononuclear cells (PBMCs) using publicly available data (*34*, *35*). We used T1D-associated gene sets from two studies that performed gene expression analysis using microarray (*34*) and single-cell RNA-seq (*35*) technologies across distinct cohorts of patients with T1D. In the first study (*34*), the authors performed microarray analysis on bulk PBMCs composed of all immune cell types from 43 patients with newly diagnosed T1D and compared them with patients with newly diagnosed T2D. Our enrichment analysis revealed that genes highly expressed in total PBMCs of patients with T1D were enriched in genes up-regulated in the disease-associated CD4 T cell cluster 2 from the spleens of T1D donors but not cluster 3 from the PLNs (fig. S10E). Moreover, genes highly expressed in total PBMCs of patients with T1D were highly enriched in genes up-regulated in the spleens of T1D-associated B cell clusters 3, 6, and 7 (fig. S10F). In the second study (*35*), the authors generated single-cell transcriptomic data from PBMCs of 46 T1D cases and 31 matched controls ["data file S3" in (*35*)]. Notably, the top differentially expressed genes associated with T1D in CD4 T cells from these data were enriched in genes up-regulated in the disease-associated CD4 T cell cluster 2 from the spleens but not cluster 3 from the PLNs (fig. S10E). Moreover, the top differentially expressed genes associated with T1D in peripheral B cells from the dataset generated by Honardoost *et al.* were enriched in genes up-regulated in the T1D-associated B cell clusters 3, 6, and 7 of the spleens (fig. S10F). Together, our cross-validation investigations across independent cohorts suggest that the enrichment of molecular features of T1D detected in the spleens can be detected in circulation.

DISCUSSION

Here, we report a distinct subset of CD4 T cells with elevated expression of *NFKB1* and *BACH2*, accompanied by chromatin remodeling

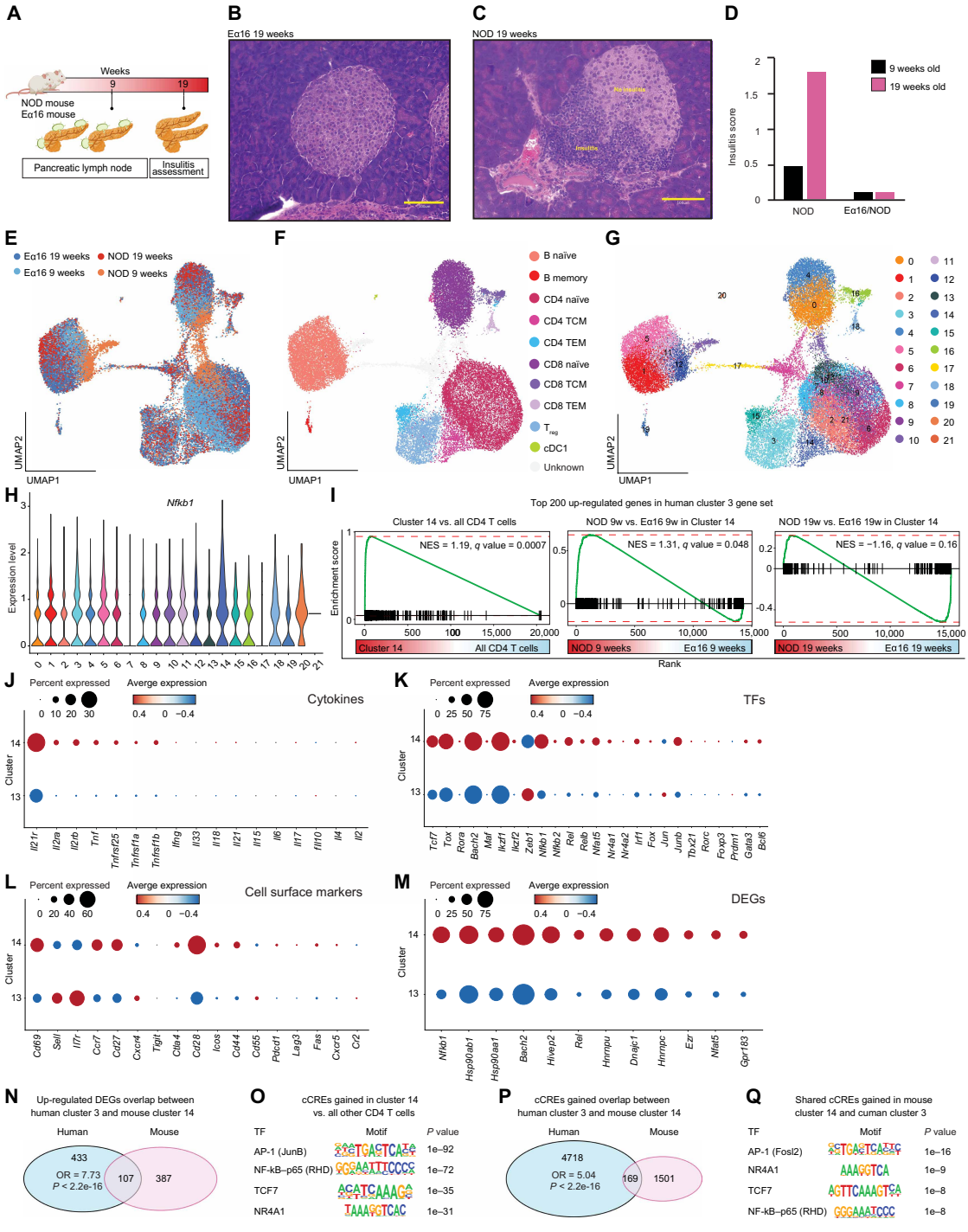

Fig. 7. *NFKB1*^{high}*BACH2*^{high} CD4 T cells representing active T1D in human PLNs are detected during presymptomatic stages in NOD mice. (**A**) Schematic outlining the experimental approach for NOD mice. (**B** and **C**) Diagrams depict representative pancreatic islets from a female 19-week-old Eα16 (B) and a littermate 19-week-old diabetic NOD mouse (C). (**D**) Bar chart indicating the insulitis score determined for each mouse. (**E** to **G**) UMAPs representing immune cells remaining after quality control analysis labeled with mouse age and strain (E), immune cell annotation (F), and cluster number (G). (**H**) Violin plot shows *Nfkb1* expression across clusters. (**I**) Preranked GSEA assessing the enrichment of the top 200 up-regulated genes in cells forming cluster 3 in human PLNs among genes up-regulated in cells forming cluster 14 in NOD mice. (**J** to **M**) Heatmaps showing the expression of cytokines (J), transcription factors (K), cell surface markers (L), and top differentially expressed genes in cluster 14 compared with all other CD4 T cells (M). (**N**) Venn diagram indicating the number of common differentially expressed genes between cluster 3 in human PLNs and cluster 14 in mouse PLNs. Fisher's exact test, odds ratio (OR) of 7.73, $P < 2.2 \times 10^{-16}$. (**O**) Seqlogo depicting de novo motif analysis using Homer in differentially accessible chromatin regions in mouse cluster 14 compared with all other CD4 T cells. (**P**) Venn diagram indicating the number of gained cCREs overlap between mouse cluster 14 and human cluster 3. Fisher's exact test, OR of 5.04, $P < 2.2 \times 10^{-16}$. (**Q**) Seqlogo depicting de novo motif analysis using Homer in shared gained accessible chromatin regions between mouse cluster 14 and human cluster 3.

linked to these transcription factors, in the PLNs of human organ donors representing active T1D. We also show an *Nfkb1*^{high}*Bach2*^{high} CD4 T cell subset in the PLNs of NOD mice at presymptomatic stages with extensive gene expression and epigenetic similarities to the human CD4 T cell subset. Although our data strongly indicate the existence of this CD4 T cell subset during the active stages of T1D, the specific identity and function of these cells remain unknown. These CD4 T cells lack the expression of cytokines and represent the expression of memory markers, suggesting that these cells are not naïve cells. The absence of T_{reg} cell–associated marker genes further excludes a regulatory role. On the basis of their cytokine-deficient profile, moderate *TCF7* expression (encoding TCF-1 protein), and high *BACH2* levels, we speculate that these CD4 T cells may represent the autoimmune progenitor pool (*9*, *36*).

TCF-1^{high} CD8$^+$ T cells with self-renewal properties have extensively been studied in chronic infection and cancer. However, we did not find previously reported gene signatures of these subsets to be enriched in our CD4 T cell population. The importance of TCF-1^{high} CD8$^+$ T cells or TCF-1^{high} CD4 T cells driving T1D has also been examined using the NOD model, although these studies did not report the expression of *Nfkb1* in cells representing the stem-like T cell subsets (*9*, *36*). *Bach2* can induce *Tcf7*, controlling stem-like CD8$^+$ T cells (*27*). In CD4 T cells, *Bach2* restrains effector responses (*26*), suggesting that, in our setting, *BACH2* may suppress cytokine expression in CD4 T cells representing cluster 3. *NFKB1* expression might be induced by T cell receptor activation (*NR4A* and *NFAT*), although it is possible that cytokines such as TL1A, a TNF family protein whose receptor DR3 is expressed in these cells (i.e., cluster 3), act as the upstream signal for *NFKB1*. The expression of *NFKB1* and *NR4A1* genes in stem-like TCF-1^{high} CD8$^+$ T cells can be found in studies focusing on these cells. The enrichment of motifs associated with NF-kB transcription factor family members within the open chromatin regions of stem-like CD8$^+$ T cells has been reported (*37*). Moreover, the increased expression of *Nfkb1*, *Rel*, and *Nr4a1/2* in exhausted precursor TCF-1^{high} CD8$^+$ T cells has been reported using single-cell RNA-seq (*38*). Our data suggest that the CD4 T cell subset in T1D PLNs is distinct from previously described TCF-1^{high} CD8$^+$ T cells, highlighting potentially unique mechanisms contributing to their identity and function. Additional mechanistic investigations in the NOD model may reveal the functional importance of these CD4 T cells.

Our focus on memory B and T cells in the spleens identified distinct enrichment of cells from AAb$^+$ and T1D donors and the potential detection of these cells in circulation. B cells in the spleens of most AAb$^+$ and T1D donors were transcriptionally and epigenetically distinct from memory B cells of HDs, and such disease-specific B cells have an elevated interferon signature. Whether these different aspects of immunity in T1D may contribute to the autoimmune process or, alternately, represent secondary effects of the altered environment in autoimmunity remains to be evaluated. Genes highly expressed in T1D-specific B and T cell clusters of the spleens could be detected in peripheral blood of T1D donors on the basis of publicly available data collected by independent groups. These results are in alignment with reports suggesting changes in B cells from peripheral blood of patients with recent-onset T1D (*39*, *40*). Together, our study suggests the importance of understanding the molecular features of immune cells in the spleen, because they can inform the development of blood-based biomarkers.

A limitation of our study is that most of AAb$^+$ donors harbored only a single autoantibody, which may represent nonprogressive islet autoimmunity. Nonetheless, our goal in this work was to leverage the HPAP dataset to generate hypotheses and establish a foundational resource for the field. In this regard, we view our study as a hypothesis-generating contribution that provides a framework for future cross-cohort analyses, biomarker discovery efforts, and flow cytometry–based validation studies.

MATERIALS AND METHODS

Study design

In this study, we conducted a comprehensive analysis of gene expression and chromatin accessibility in nearly 1 million immune cells from the pancreatic lymph nodes and spleens of 43 individuals with and without T1D. We found a distinct subset of CD4$^+$ T cells selectively present in the pancreatic lymph nodes of organ donors representing the active disease stage. These cells exhibited elevated activity of *NFKB1* and *BACH2*, along with extensive chromatin remodeling associated with these transcription factors. These findings were subsequently corroborated in a T1D mouse model.

Human participants

PLNs and spleens were obtained through the HPAP consortium (RRID:SCR_016202; https://hpap.pmacs.upenn.edu), a component of the Human Islet Research Network (https://hirnetwork.org). Procurement was conducted under approval from the University of Florida Institutional Review Board (IRB no. 201600029) and the United Network for Organ Sharing. Informed consent for organ retrieval was obtained from a legal representative of each donor. T1D diagnosis was confirmed through medical chart review and measurement of C-peptide levels following American Diabetes Association guidelines. All donors were screened for islet autoantibodies before organ recovery, and autoantibody positivity was verified after tissue processing and islet isolation.

NOD mice

NOD/ShiLtJ (NOD) mice were obtained from the Jackson Laboratory. We used age- and sex-matched Eα16/NOD littermates, which are genetically identical to the NOD strain except for a targeted modification that enables the expression of the MHC class II Eα transcript, conferring protection against T1D (*30*–*33*). Eα16/NOD mice were obtained from the Silverman laboratory. Littermate female mice of 9 and 19 weeks old were used in the study. The animal work was done based on the Institutional Animal Care and Use Committee of the University of Pennsylvania and the Children Hospital of Pennsylvania in accordance with NIH guidelines. Insulitis was assessed following dissection of the pancreases, which were fixed in 10% formalin. The fixed tissue was embedded in paraffin, sectioned, and stained with hematoxylin and eosin. At least 75 pancreatic islets per mouse were scored under bright field microscopy by two examiners blinded to the identity of the samples. Scores for each islet ranged from 0 to 2; 0 indicates the absence of insulitis, 1 denotes peri-insulitis or the presence of leukocytes within the periphery of the islets, and 2 signifies the filtration of leukocytes into the islets. The insulitis score represents the mean insulitis value for all of the islets evaluated from each mouse pancreas.

Tissue processing

R10 medium [500 ml of RPMI medium 1640 (Gibco/Invitrogen), 10% fetal bovine serum, penicillin (100 U/ml), and 2 mM L-glutamine] with

50 μl of deoxyribonuclease (DNase) I (Thermo Fisher Scientific, catalog no. EN0521) was prepared. The fat tissue around PLN tissues was cut away in a dish, and the tissue was rinsed with the prepared medium. The PLN tissues were cut into small pieces and placed in the 70-μm strainer into a dish and smashed using the top end of a 5-ml syringe. The medium consisting of PLN cells was strained through the 70-μm strainer into a 50-ml conical tube. The cells were centrifuged at 800*g* for 5 min. The cells were washed again with R10 medium and counted. After centrifugation, the cells were resuspended in freezing medium (Gibco, catalog no. 12648010) and stored in Mr. Frosty (Nalgene, catalog no. 5100-0001) freezing container at −80°C for 1 day, and, then, they were transferred to a liquid nitrogen tank (Thermo Fisher Scientific). For spleen tissue, 50 μl of DNase and 50 μl of collagenase D (Roche, catalog no. 11088866001) have been added to 50 ml of R10 medium. The spleen tissue was cut into small pieces and transferred to the gentleMACS C tube (MACS Miltenyi, catalog no. 130-093-237) with medium. After dissociation, the dissociated tissue was smashed through a 100-μm strainer using the top end of a 5-ml syringe into a dish. The medium consisting of spleen cells was strained through the 100-μm strainer into a 50-ml conical tube. The cells were centrifuged and 5 ml of ACK (ammonium-chloride-potassium) lysis buffer (Quality Biological, catalog no. 118-156-721) was added to lysis red blood cells and incubated for 5 min. Then, R10 medium was added to the cells, and the cells were centrifuged at 800*g* for 5 min. The cell pellets were resuspended in R10 medium and counted. After centrifugation, the cells were resuspended in freezing medium and stored in a Mr. Frosty at −80°C for 1 day, and, then, they were transferred to a liquid nitrogen tank. For NOD mice, PLNs were harvested and placed in the 70-μm strainer in a 50-ml conical tube and smashed using the top end of a 5-ml syringe. The cells were washed with medium and counted.

IF experiments and image analysis

In our microscopy experiments, microscope make and model was Leica DMi8CEL Advanced inverted Microscope; the imaging modality was confocal laser scanning microscopy; autofocus system was Leica LAS X Adaptive Focus Control, the objective lens specifications were 63×/1.4 oil immersion; the imaging environmental conditions was slides in dark at room temperature; the fluorescent filters were filter cubes configured for 4′,6-diamidino-2-phenylindole (DAPI), fluorescein isothiocyanate, and tetramethyl rhodamine isothiocyanate; the laser lines were multiline laser module (e.g., 405, 488, 561, and 633 nm); the camera/detector type was photomultiplier tubes and hybrid detectors; the motorized components were motorized XY stage, focus drive, and objective turret; the image acquisition software was Leica LAS X (Leica Application Suite X), version 3.5.7; and the image processing software was LAS X.

The lymph nodes were harvested from the peripancreatic tissues of organ donors. The samples were fixed in 10% formalin (24 ± 8 hours) and then embedded in paraffin. The tissue blocks were manually sectioned using a microtome to obtain 5-μm slices. For IF staining, after dewaxing, the slides were boiled in a citrate buffer at pH 6.0 for 20 min to repair the antigens. After incubation with the blocking buffer at room temperature for 1 hour, the slides were incubated overnight at 4°C with the antibody at the optimal dilution. The antibodies used were NFKB1 (Proteintech, Rosemont, IL) and CD4 and CD45RO (Abcam, Cambridge, MA), separately. All slides were washed in the washing buffer and then incubated for 1 hour with the tyramide signal amplification kit (Thomas Scientific, Swedesboro, NJ) for secondary antibody incubation for CD4 and NFKB1 antibodies. Tyramide conjugate was added to 0.03% H_2O_2 in phosphate-buffered saline (PBS) and incubated in the dark at room temperature for 10 min. Last, the slides were washed and sealed with ProLong Gold reagent containing DAPI before scanning (Invitrogen, catalog no. P10144).

Intensity measurements of IF-stained HPAP tissues were performed using Fiji (*41*). First, to account for technical variation in signal intensity between different tissue sections, "Quantile-Based Normalization" plugin was used to normalize the distribution of pixel values across the CD4, CD45RO, and NFkB1 channels for each tissue ("Plugins" → "Process" → "Quantile-Based Normalization"). For each of the three channels, the quantiles were replaced with "Mean" pixel values without rescaling the original image.

Cell segmentation was completed using the "MorphoLibJ" plugin (*42*). Images of the CD4, CD45RO, and NFkB1 channels were first converted to 8-bit gray images and subtracted for background signal ("Process" → "Subtract background") with a "rolling ball radius" of 10 pixels with "Sliding paraboloid" enabled. Watershed segmentation was performed with the input images classified as "border image" with a tolerance of "30" selected to increase the stringency of segmentation and reduce oversegmentation. Results of segmentation were displayed as "Watershed lines" on the original input image. Cell annotation was performed using the "Analyze Particles" tool with a 'size' of 50– to 6000–square pixel area and a "circularity" within the range 0 to 1.00. Cell annotations were added to the "ROI manager" tool and overlaid with the CD4, CD45RO, and NFkB1 channels for each tissue. Mean intensity of annotated cells were saved to CSV files using the "Measure" function within the "ROI manager." This process was repeated for all three channels per tissue.

Segmented cells were grouped into memory $CD4^+$ $CD45RO^+$ and naïve $CD4^+$ cells (i.e., CD45RO) using R running on RStudio (version 2022.07.2 + 576). Cells were classified into the two groups on the basis of a threshold inferred from the mean intensity values of annotated cells and confirmed by visual inspection of signal morphology (i.e., radial signal pattern for both CD4 and CD45RO indicating cell surface expression). Annotated cells were first filtered using the CD4 mean intensity threshold (>53.06 for HD and >59.587 for AAb+3) and the cells that had higher intensity were subjected to a second filtering using the CD45RO mean intensity threshold (>75.746 for HD and > 74.119 for AAb+3). Cells that passed the second threshold were grouped into memory $CD4^+$ $CD45RO^+$ cells, while cells that failed were grouped as naïve $CD4^+$ T cells. NFkB1 mean intensity was plotted for both filtered groups and compared.

Fluorescence-activated cell sorting

Frozen cells were incubated in a water bath at 37°C. Thawed cells were transferred quickly to labeled 50-ml tubes consisting of 10 ml of warm R10 medium. Cells were centrifuged at 400*g* for 5 min at 4°C, and the supernatant was discarded. For the second wash, PBS (Gibco) was added to the cells, and the cells were centrifuged again. After centrifuging, 100 μl of diluted viability dye [1:500 L/D Aqua (Invitrogen, catalog no. L34957)] was added to the cells and incubated at 4°C in the dark for 20 min. After incubation time, PBS was added to the cells, and they centrifuged at 400*g* for 5 min. Cells were resuspended in 100 μl of PBS, and then 10 μl of human TruStain FcX (BioLegend, catalog no. 422302) was added and cells were incubated at 4°C in the dark for 10 min. After centrifuging, antibodies CD45 (clone HI30; BioLegend, catalog no. 304005) and CD15 (clone W6D3; BioLegend, catalog no. 323043) were diluted in PBS buffer, and the panel was added to the cells and incubated for 30 min at 4°C in the dark. Cells

were stained with 7AAD (eBioscience, no. 00-6993-50) for live cell staining 10 min before sorting. Cells were washed and resuspended in PBS. Cells were sorted on a FACSAria fusion I using FACSDiva software 8.0.2 (BD Biosciences). Cells were sorted to collect live $CD45^+$ $CD15^-$ cells.

For mice PLNs, cells were incubated with 100 μl of diluted viability dye (1:500 L/D Aqua, Invitrogen) for 20 min at 4°C in the dark. After incubation, cells were washed once with PBS and centrifuged at 400*g* for 5 min. The pellet was resuspended in 100 μl of PBS, followed by addition of 10 μl of mouse TruStain FcX (BioLegend, catalog no. 101319) and incubation for 10 min at 4°C in the dark. Cells were then stained with antibodies against CD45 (clone 30-F11; BioLegend, catalog no. 103133) and CD15 (clone MC-480; BioLegend, catalog no. 125617) diluted in PBS for 30 min at 4°C in the dark. Ten minutes before sorting, 7AAD (eBioscience) was added for live/dead discrimination. Live $CD45^+$ $CD15^-$ cells were sorted on a FACSAria II (BD Biosciences).

Single Cell Multiome ATAC + Gene Expression

Single-cell multiome data were generated using Chromium Next GEM Single Cell Multiome ATAC + Gene Expression kit (10x Genomics). Nucleus isolation with some modifications was performed on the basis of the 10x Protocol (CG000365). The modifications in the nucleus isolation protocol were as follows. Diluted lysis buffer was made using 400 μl of diluted lysis solution [10 mM NaCl, 10 mM tris-HCl (pH 7.4), 3 mM $MgCl_2$, 1 mM dithiothreitol, 1% bovine serum albumin, ribonuclease inhibitor (1 U/μl), and nuclease-free water] and 200 μl of lysis buffer (CG000368), and the cells were incubated on ice with the 100 μl of diluted lysis buffer. The rest of the protocols were followed on the basis of the manufacturer's instructions. The quality of libraries was assessed using TapeStation 2200 (Agilent) and quantified using Kapa (Roche, catalog no. 07960140001). The sequencing was performed on the NovaSeq6000 (Illumina). Bcl2fastq conversion and sample aggregation were performed using Cell Ranger ARC 2.0.2 (10x Genomics).

Hashtag antibody staining

For donors which were added to create the age-matched cohort, we used hashtag (HTO) antibodies (BioLegend, catalog nos. 394601, 394603, 394605, 394607, 394609, 394611, 394613, and 394615) to multiplex PLN samples for single-cell multiome. Cells were stained with hashtag antibody for 30 min at 4°C and washed with PBS. Hashtag library was prepared according to the TEA-seq protocol and was sequenced with RNA library. Counts for HTO library were obtained using 10x Cell Ranger multi. HTO counts were normalized using the centered log ratio (CLR) transformation.

TEA-seq

After thawing the cells, the TEA-seq protocol (*16*) was used to stain the cells with TotalSeq A cocktail antibody (BioLegend, catalog no. 399907) according to the manufacturer's instructions. The required oligos were obtained from the TEA-seq protocol and were ordered from Integrated DNA Technologies. The modifications to multiome assay to obtain the antibody-derived tag (ADT) library along with RNA and ATAC modalities were performed on the basis of the TEA-seq protocol. To process single-cell ADT, BarCounter (https://github.com/AllenInstitute/Barcounter-release) was used, and ADT counting was performed on the basis of the software guideline. ADT counts were normalized using the CLR transformation. After adding ADT modality to the multiome object, the dataset was processed using our multiome pipeline.

Statistical analysis

Statistical analysis is available in the Supplementary Materials.

Supplementary Materials

The PDF file includes:
Supplementary Text
Figs. S1 to S10
References (*44*–*62*)

Other Supplementary Material for this manuscript includes the following:
Data files S1 to S6
MDAR Reproducibility Checklist

REFERENCES AND NOTES

1. J. T. Warshauer, J. A. Bluestone, M. S. Anderson, New frontiers in the treatment of type 1 diabetes. *Cell Metab.* **31**, 46–61 (2020).
2. M. Waibel, J. M. Wentworth, M. So, J. J. Couper, F. J. Cameron, R. MacIsaac, G. Atlas, A. Gorelik, S. Litwak, L. Sanz-Villanueva, P. Trivedi, S. Ahmed, F. J. Martin, M. E. Doyle, J. E. Harbison, C. Hall, B. Krishnamurthy, P. G. Colman, L. C. Harrison, H. E. Thomas, T. W. H. Kay, BANDIT Study Group, Baricitinib and β-cell function in patients with new-onset type 1 diabetes. *N. Engl. J. Med.* **389**, 2140–2150 (2023).
3. T. Quattrin, M. J. Haller, A. K. Steck, E. I. Felner, Y. Li, Y. Xia, J. H. Leu, R. Zoka, J. A. Hedrick, M. R. Rigby, F. Vercruysse, T1GER Study Investigators, Golimumab and beta-cell function in youth with new-onset type 1 diabetes. *N. Engl. J. Med.* **383**, 2007–2017 (2020).
4. E. L. Ramos, C. M. Dayan, L. Chatenoud, Z. Sumnik, K. M. Simmons, A. Szypowska, S. E. Gitelman, L. A. Knecht, E. Niemoeller, W. Tian, K. C. Herold, PROTECT Study Investigators, Teplizumab and β-cell function in newly diagnosed type 1 diabetes. *N. Engl. J. Med.* **389**, 2151–2161 (2023).
5. K. H. Kaestner, A. C. Powers, A. Naji, HPAP Consortium, M. A. Atkinson, NIH initiative to improve understanding of the pancreas, islet, and autoimmunity in type 1 diabetes: The Human Pancreas Analysis Program (HPAP). *Diabetes* **68**, 1394–1402 (2019).
6. S. N. Shapira, A. Naji, M. A. Atkinson, A. C. Powers, K. H. Kaestner, Understanding islet dysfunction in type 2 diabetes through multidimensional pancreatic phenotyping: The human pancreas analysis program. *Cell Metab.* **34**, 1906–1913 (2022).
7. M. Fasolino, G. W. Schwartz, A. R. Patil, A. Mongia, M. L. Golson, Y. J. Wang, A. Morgan, C. Liu, J. Schug, J. Liu, M. Wu, D. Traum, A. Kondo, C. L. May, N. Goldman, W. Wang, M. Feldman, J. H. Moore, A. S. Japp, M. R. Betts, the HPAP Consortium, M. Fasolino, G. W. Schwartz, A. R. Patil, A. Mongia, M. L. Golson, Y. J. Wang, A. Morgan, C. Liu, J. Schug, J. Liu, M. Wu, D. Traum, A. Kondo, C. L. May, N. Goldman, W. Wang, M. Feldman, J. H. Moore, A. S. Japp, M. R. Betts, R. B. Faryabi, A. Naji, K. H. Kaestner, G. Vahedi, R. B. Faryabi, A. Naji, K. H. Kaestner, G. Vahedi, Single-cell multi-omics analysis of human pancreatic islets reveals novel cellular states in type 1 diabetes. *Nat. Metab.* **4**, 284–299 (2022).
8. M. C. Gagnerault, J. J. Luan, C. Lotton, F. Lepault, Pancreatic lymph nodes are required for priming of beta cell reactive T cells in NOD mice. *J. Exp. Med.* **196**, 369–377 (2002).
9. S. V. Gearty, F. Dündar, P. Zumbo, G. Espinosa-Carrasco, M. Shakiba, F. J. Sanchez-Rivera, N. D. Socci, P. Trivedi, S. W. Lowe, P. Lauer, N. Mohibullah, A. Viale, T. P. DiLorenzo, D. Betel, A. Schietinger, An autoimmune stem-like CD8 T cell population drives type 1 diabetes. *Nature* **602**, 156–161 (2022).
10. Y. Hao, S. Hao, E. Andersen-Nissen, W. M. Mauck III, S. Zheng, A. Butler, M. J. Lee, A. J. Wilk, C. Darby, M. Zager, P. Hoffman, M. Stoeckius, E. Papalexi, E. P. Mimitou, J. Jain, A. Srivastava, T. Stuart, L. M. Fleming, B. Yeung, A. J. Rogers, J. M. McElrath, C. A. Blish, R. Gottardo, P. Smibert, R. Satija, Integrated analysis of multimodal single-cell data. *Cell* **184**, 3573–3587.e29 (2021).
11. A. R. Patil, J. Schug, A. Naji, K. H. Kaestner, R. B. Faryabi, G. Vahedi, Single-cell expression profiling of islets generated by the human pancreas analysis program. *Nat. Metab.* **5**, 713–715 (2023).
12. I. Korsunsky, N. Millard, J. Fan, K. Slowikowski, F. Zhang, K. Wei, Y. Baglaenko, M. Brenner, P. R. Loh, S. Raychaudhuri, Fast, sensitive and accurate integration of single-cell data with Harmony. *Nat. Methods* **16**, 1289–1296 (2019).
13. M. D. Luecken, M. Büttner, K. Chaichoompu, A. Danese, M. Interlandi, M. F. Mueller, D. C. Strobl, L. Zappia, M. Dugas, M. Colomé-Tatché, F. J. Theis, Benchmarking atlas-level data integration in single-cell genomics. *Nat. Methods* **19**, 41–50 (2022).
14. Z. Zhang, D. Mathew, T. L. Lim, K. Mason, C. M. Martinez, S. Huang, E. J. Wherry, K. Susztak, A. J. Minn, Z. Ma, N. R. Zhang, Recovery of biological signals lost in single-cell batch integration with CellANOVA. *Nat. Biotechnol.* 10.1038/s41587-024-02463-1 (2024).

15. M. Lotfollahi, M. Naghipourfar, M. D. Luecken, M. Khajavi, M. Büttner, M. Wagenstetter, Ž. Avsec, A. Gayoso, N. Yosef, M. Interlandi, S. Rybakov, A. V. Misharin, F. J. Theis, Mapping single-cell data to reference atlases by transfer learning. *Nat. Biotechnol.* **40**, 121–130 (2022).
16. E. Swanson, C. Lord, J. Reading, A. T. Heubeck, P. C. Genge, Z. Thomson, M. D. A. Weiss, X. J. Li, A. K. Savage, R. R. Green, T. R. Torgerson, T. F. Bumol, L. T. Graybuck, P. J. Skene, Simultaneous trimodal single-cell measurement of transcripts, epitopes, and chromatin accessibility using TEA-seq. *eLife* **10**, e63632 (2021).
17. A. Subramanian, P. Tamayo, V. K. Mootha, S. Mukherjee, B. L. Ebert, M. A. Gillette, A. Paulovich, S. L. Pomeroy, T. R. Golub, E. S. Lander, J. P. Mesirov, Gene set enrichment analysis: A knowledge-based approach for interpreting genome-wide expression profiles. *Proc. Natl. Acad. Sci. U.S.A.* **102**, 15545–15550 (2005).
18. H. Kallionpää, L. L. Elo, E. Laajala, J. Mykkänen, I. Ricaño-Ponce, M. Vaarma, T. D. Laajala, H. Hyöty, J. Ilonen, R. Veijola, T. Simell, C. Wijmenga, M. Knip, H. Lähdesmäki, O. Simell, R. Lahesmaa, Innate immune activity is detected prior to seroconversion in children with HLA-conferred type 1 diabetes susceptibility. *Diabetes* **63**, 2402–2414 (2014).
19. R. C. Ferreira, H. Guo, R. M. R. Coulson, D. J. Smyth, M. L. Pekalski, O. S. Burren, A. J. Cutler, J. D. Doecke, S. Flint, E. F. McKinney, P. A. Lyons, K. G. C. Smith, P. Achenbach, A. Beyerlein, D. B. Dunger, D. G. Clayton, L. S. Wicker, J. A. Todd, E. Bonifacio, C. Wallace, A. G. Ziegler, A type I interferon transcriptional signature precedes autoimmunity in children genetically at risk for type 1 diabetes. *Diabetes* **63**, 2538–2550 (2014).
20. A. Jay, C. M. Pondevida, G. Vahedi, The epigenetic landscape of fate decisions in T cells. *Nat. Immunol.* **26**, 544–556 (2025).
21. E. P. Consortium, J. E. Moore, M. J. Purcaro, H. E. Pratt, C. B. Epstein, N. Shoresh, J. Adrian, T. Kawli, C. A. Davis, A. Dobin, R. Kaul, J. Halow, E. L. Van Nostrand, P. Freese, D. U. Gorkin, Y. Shen, Y. He, M. Mackiewicz, F. Pauli-Behn, B. A. Williams, A. Mortazavi, C. A. Keller, X.-O. Zhang, S. I. Elhajjajy, J. Huey, D. E. Dickel, V. Snetkova, X. Wei, X. Wang, J. C. Rivera-Mulia, J. Rozowsky, J. Zhang, S. B. Chhetri, J. Zhang, A. Victorsen, K. P. White, A. Visel, G. W. Yeo, C. B. Burge, E. Lécuyer, D. M. Gilbert, J. Dekker, J. Rinn, E. M. Mendenhall, J. R. Ecker, M. Kellis, R. J. Klein, W. S. Noble, A. Kundaje, R. Guigó, P. J. Farnham, J. M. Cherry, R. M. Myers, B. Ren, B. R. Graveley, M. B. Gerstein, L. A. Pennacchio, M. P. Snyder, B. E. Bernstein, B. Wold, R. C. Hardison, T. R. Gingeras, J. A. Stamatoyannopoulos, Z. Weng, Expanded encyclopaedias of DNA elements in the human and mouse genomes. *Nature* **583**, 699–710 (2020).
22. V. Atsaves, V. Leventaki, G. Z. Rassidakis, F. X. Claret, AP-1 transcription factors as regulators of immune responses in cancer. *Cancers* **11**, 1037 (2019).
23. C. A. de Leeuw, J. M. Mooij, T. Heskes, D. Posthuma, MAGMA: Generalized gene-set analysis of GWAS data. *PLoS Comput. Biol.* **11**, e1004219 (2015).
24. K. K. Farh, A. Marson, J. Zhu, M. Kleinewietfeld, W. J. Housley, S. Beik, N. Shoresh, H. Whitton, R. J. H. Ryan, A. A. Shishkin, M. Hatan, M. J. Carrasco-Alfonso, D. Mayer, C. J. Luckey, N. A. Patsopoulos, P. L. de Jager, V. K. Kuchroo, C. B. Epstein, M. J. Daly, D. A. Hafler, B. E. Bernstein, Genetic and epigenetic fine mapping of causal autoimmune disease variants. *Nature* **518**, 337–343 (2015).
25. B. M. Bolstad, R. A. Irizarry, M. Astrand, T. P. Speed, A comparison of normalization methods for high density oligonucleotide array data based on variance and bias. *Bioinformatics* **19**, 185–193 (2003).
26. R. Roychoudhuri, K. Hirahara, K. Mousavi, D. Clever, C. A. Klebanoff, M. Bonelli, G. Sciumè, H. Zare, G. Vahedi, B. Dema, Z. Yu, H. Liu, H. Takahashi, M. Rao, P. Muranski, J. G. Crompton, G. Punkosdy, D. Bedognetti, E. Wang, V. Hoffmann, J. Rivera, F. M. Marincola, A. Nakamura, V. Sartorelli, Y. Kanno, L. Gattinoni, A. Muto, K. Igarashi, J. J. O'Shea, N. P. Restifo, BACH2 represses effector programs to stabilize T_{reg}-mediated immune homeostasis. *Nature* **498**, 506–510 (2013).
27. C. Yao, G. Lou, H. W. Sun, Z. Zhu, Y. Sun, Z. Chen, D. Chauss, E. A. Moseman, J. Cheng, M. A. D'Antonio, W. Shi, J. Shi, K. Kometani, T. Kurosaki, E. J. Wherry, B. Afzali, L. Gattinoni, Y. Zhu, D. B. McGavern, J. J. O'Shea, P. L. Schwartzberg, T. Wu, BACH2 enforces the transcriptional and epigenetic programs of stem-like $CD8^+$ T cells. *Nat. Immunol.* **22**, 370–380 (2021).
28. K. Y. Chen, K. Y. Chen, M. De Giovanni, Y. Xu, J. An, N. Kirthivasan, E. Lu, K. Jiang, S. Brooks, S. Ranucci, J. Yang, S. Kanameishi, K. Kabashima, K. Brulois, M. Bscheider, E. C. Butcher, J. G. Cyster, Inflammation switches the chemoattractant requirements for naive lymphocyte entry into lymph nodes. *Cell* **188**, 1019–1035.e22 (2024).
29. C. B. González-Blas, S. De Winter, G. Hulselmans, N. Hecker, I. Matetovici, V. Christiaens, S. Poovathingal, J. Wouters, S. Aibar, S. Aerts, SCENIC+: Single-cell multiomic inference of enhancers and gene regulatory networks. *Nat. Methods* **20**, 1355–1367 (2023).
30. M. Silverman, L. Kua, A. Tanca, M. Pala, A. Palomba, C. Tanes, K. Bittinger, S. Uzzau, C. Benoist, D. Mathis, Protective major histocompatibility complex allele prevents type 1 diabetes by shaping the intestinal microbiota early in ontogeny. *Proc. Natl. Acad. Sci. U.S.A.* **114**, 9671–9676 (2017).
31. H. Nishimoto, H. Kikutani, K. Yamamura, T. Kishimoto, Prevention of autoimmune insulitis by expression of I-E molecules in NOD mice. *Nature* **328**, 432–434 (1987).
32. J. Bohme, B. Schuhbaur, O. Kanagawa, C. Benoist, D. Mathis, MHC-linked protection from diabetes dissociated from clonal deletion of T cells. *Science* **249**, 293–295 (1990).
33. M. Le Meur, P. Gerlinger, C. Benoist, D. Mathis, Correcting an immune-response deficiency by creating E_α gene transgenic mice. *Nature* **316**, 38–42 (1985).
34. E. C. Kaizer, C. L. Glaser, D. Chaussabel, J. Banchereau, V. Pascual, P. C. White, Gene expression in peripheral blood mononuclear cells from children with diabetes. *J. Clin. Endocrinol. Metab.* **92**, 3705–3711 (2007).
35. M. A. Honardoost, A. Adinatha, F. Schmidt, B. Ranjan, M. Ghaeidamini, N. Arul Rayan, M. Gek Liang Lim, I. Joanito, Q. Xiao Xuan Lin, D. Rajagopalan, S. Qi Mok, Y. Y. Hwang, A. Larbi, C. C. Khor, R. Foo, B. O. Boehm, S. Prabhakar, Systematic immune cell dysregulation and molecular subtypes revealed by single-cell RNA-seq of subjects with type 1 diabetes. *Genome Med.* **16**, 45 (2024).
36. N. Aljobaily, D. Allard, B. Perkins, A. Raugh, T. Galland, Y. Jing, W. Z. Stephens, M. L. Bettini, J. S. Hale, M. Bettini, Autoimmune $CD4^+$ T cells fine-tune TCF1 expression to maintain function and survive persistent antigen exposure during diabetes. *Immunity* **57**, 2583–2596.e6 (2024).
37. R. R. Jadhav, S. J. Im, B. Hu, M. Hashimoto, P. Li, J. X. Lin, W. J. Leonard, W. J. Greenleaf, R. Ahmed, J. J. Goronzy, Epigenetic signature of PD-1+ TCF1+ CD8 T cells that act as resource cells during chronic viral infection and respond to PD-1 blockade. *Proc. Natl. Acad. Sci. U.S.A.* **116**, 14113–14118 (2019).
38. Z. Chen, Z. Ji, S. F. Ngiow, S. Manne, Z. Cai, A. C. Huang, J. Johnson, R. P. Staupe, B. Bengsch, C. Xu, S. Yu, M. Kurachi, R. S. Herati, L. A. Vella, A. E. Baxter, J. E. Wu, O. Khan, J. C. Beltra, J. R. Giles, E. Stelekati, L. M. McLane, C. W. Lau, X. Yang, S. L. Berger, G. Vahedi, H. Ji, E. J. Wherry, TCF-1-centered transcriptional network drives an effector versus exhausted CD8 T cell-fate decision. *Immunity* **51**, 840–855.e5 (2019).
39. M. J. Smith, T. A. Packard, S. K. O'Neill, C. J. Henry Dunand, M. Huang, L. Fitzgerald-Miller, D. Stowell, R. M. Hinman, P. C. Wilson, P. A. Gottlieb, J. C. Cambier, Loss of anergic B cells in prediabetic and new-onset type 1 diabetic patients. *Diabetes* **64**, 1703–1712 (2015).
40. Z. C. Stensland, C. A. Magera, H. Broncucia, B. D. Gomez, N. M. Rios-Guzman, K. L. Wells, C. A. Nicholas, M. Rihanek, M. J. Hunter, K. P. Toole, P. A. Gottlieb, M. J. Smith, Identification of an anergic BND cell-derived activated B cell population (BND2) in young-onset type 1 diabetes patients. *J. Exp. Med.* **220**, (2023).
41. J. Schindelin, I. Arganda-Carreras, E. Frise, V. Kaynig, M. Longair, T. Pietzsch, S. Preibisch, C. Rueden, S. Saalfeld, B. Schmid, J. Y. Tinevez, D. J. White, V. Hartenstein, K. Eliceiri, P. Tomancak, A. Cardona, Fiji: An open-source platform for biological-image analysis. *Nat. Methods* **9**, 676–682 (2012).
42. D. Legland, I. Arganda-Carreras, P. Andrey, MorphoLibJ: Integrated library and plugins for mathematical morphology with ImageJ. *Bioinformatics* **32**, 3532–3534 (2016).
43. P. Rai, Cross-species multiome profiling of lymphoid tissues reveals gene regulatory changes in type 1 diabetes, version v1, Zenodo (2025); https://doi.org/10.5281/zenodo.16696694.
44. P. L. Germain, A. Lun, C. Garcia Meixide, W. Macnair, M. D. Robinson, Doublet identification in single-cell sequencing data using scDblFinder. *F1000Res* **10**, 979 (2021).
45. C. Hafemeister, R. Satija, Normalization and variance stabilization of single-cell RNA-seq data using regularized negative binomial regression. *Genome Biol.* **20**, 296 (2019).
46. C. Hu, T. Li, Y. Xu, X. Zhang, F. Li, J. Bai, J. Chen, W. Jiang, K. Yang, Q. Ou, X. Li, P. Wang, Y. Zhang, CellMarker 2.0: An updated database of manually curated cell markers in human/mouse and web tools based on scRNA-seq data. *Nucleic Acids Res.* **51**, D870–D876 (2023).
47. Y. Zhang, T. Liu, C. A. Meyer, J. Eeckhoute, D. S. Johnson, B. E. Bernstein, C. Nusbaum, R. M. Myers, M. Brown, W. Li, X. S. Liu, Model-based analysis of ChIP-Seq (MACS). *Genome Biol.* **9**, R137 (2008).
48. M. D. Robinson, D. J. McCarthy, G. K. Smyth, edgeR: A Bioconductor package for differential expression analysis of digital gene expression data. *Bioinformatics* **26**, 139–140 (2010).
49. Y. Zhou, B. Zhou, L. Pache, M. Chang, A. H. Khodabakhshi, O. Tanaseichuk, C. Benner, S. K. Chanda, Metascape provides a biologist-oriented resource for the analysis of systems-level datasets. *Nat. Commun.* **10**, 1523 (2019).
50. J. Chiou, R. J. Geusz, M. L. Okino, J. Y. Han, M. Miller, R. Melton, E. Beebe, P. Benaglio, S. Huang, K. Korgaonkar, S. Heller, A. Kleger, S. Preissl, D. U. Gorkin, M. Sander, K. J. Gaulton, Interpreting type 1 diabetes risk with genetics and single-cell epigenomics. *Nature* **594**, 398–402 (2021).
51. Y. Okada, D. Wu, G. Trynka, T. Raj, C. Terao, K. Ikari, Y. Kochi, K. Ohmura, A. Suzuki, S. Yoshida, R. R. Graham, A. Manoharan, W. Ortmann, T. Bhangale, J. C. Denny, R. J. Carroll, A. E. Eyler, J. D. Greenberg, J. M. Kremer, D. A. Pappas, L. Jiang, J. Yin, L. Ye, D.-F. Su, J. Yang, G. Xie, E. Keystone, H.-J. Westra, T. Esko, A. Metspalu, X. Zhou, N. Gupta, D. Mirel, E. A. Stahl, D. Diogo, J. Cui, K. Liao, M. H. Guo, K. Myouzen, T. Kawaguchi, M. J. H. Coenen, P. L. C. M. van Riel, M. A. F. J. van de Laar, H.-J. Guchelaar, T. W. J. Huizinga, P. Dieudé, X. Mariette, S. Louis Bridges Jr., A. Zhernakova, R. E. M. Toes, P. P. Tak, C. Miceli-Richard, S.-Y. Bang, H.-S. Lee, J. Martin, M. A. Gonzalez-Gay, L. Rodriguez-Rodriguez, S. Rantapää-Dahlqvist, L. Arlestig, H. K. Choi, Y. Kamatani, P. Galan, M. Lathrop, RACI consortium, GARNET consortium, S. Eyre, J. Bowes, A. Barton, N. de Vries, L. W. Moreland, L. A. Criswell, E. W. Karlson, A. Taniguchi, R. Yamada, M. Kubo, J. S. Liu, S.-C. Bae, J. Worthington, L. Padyukov, L. Klareskog, P. K. Gregersen, S. Raychaudhuri, B. E. Stranger,

P. L. De Jager, L. Franke, P. M. Visscher, M. A. Brown, H. Yamanaka, T. Mimori, A. Takahashi, H. Xu, T. W. Behrens, K. A. Siminovitch, S. Momohara, F. Matsuda, K. Yamamoto, R. M. Plenge, Genetics of rheumatoid arthritis contributes to biology and drug discovery. *Nature* **506**, 376–381 (2014).
52. J. Bentham, D. L. Morris, D. S. Cunninghame Graham, C. L. Pinder, P. Tombleson, T. W. Behrens, J. Martín, B. P. Fairfax, J. C. Knight, L. Chen, J. Replogle, A. C. Syvänen, L. Rönnblom, R. R. Graham, J. E. Wither, J. D. Rioux, M. E. Alarcón-Riquelme, T. J. Vyse, Genetic association analyses implicate aberrant regulation of innate and adaptive immunity genes in the pathogenesis of systemic lupus erythematosus. *Nat. Genet.* **47**, 1457–1464 (2015).
53. J. Z. Liu, S. van Sommeren, H. Huang, S. C. Ng, R. Alberts, A. Takahashi, S. Ripke, J. C. Lee, L. Jostins, T. Shah, S. Abedian, J. H. Cheon, J. Cho, N. E. Daryani, L. Franke, Y. Fuyuno, A. Hart, R. C. Juyal, G. Juyal, W. H. Kim, A. P. Morris, H. Poustchi, W. G. Newman, V. Midha, T. R. Orchard, H. Vahedi, A. Sood, J. J. Y. Sung, R. Malekzadeh, H. J. Westra, K. Yamazaki, S. K. Yang, International Multiple Sclerosis Genetics Consortium, International IBD Genetics Consortium, J. C. Barrett, A. Franke, B. Z. Alizadeh, M. Parkes, T. B K, M. J. Daly, M. Kubo, C. A. Anderson, R. K. Weersma, Association analyses identify 38 susceptibility loci for inflammatory bowel disease and highlight shared genetic risk across populations. *Nat. Genet.* **47**, 979–986 (2015).
54. L. Paternoster, M. Standl, J. Waage, H. Baurecht, M. Hotze, D. P. Strachan, J. A. Curtin, K. Bønnelykke, C. Tian, A. Takahashi, J. Esparza-Gordillo, A. C. Alves, J. P. Thyssen, H. den Dekker, M. A. Ferreira, E. Altmaier, P. M. Sleiman, F. L. Xiao, J. R. Gonzalez, I. Marenholz, B. Kalb, M. P. Yanes, C. J. Xu, L. Carstensen, M. M. Groen-Blokhuis, C. Venturini, C. E. Pennell, S. J. Barton, A. M. Levin, I. Curjuric, M. Bustamante, E. Kreiner-Møller, G. A. Lockett, J. Bacelis, S. Bunyavanich, R. A. Myers, A. Matanovic, A. Kumar, J. Y. Tung, T. Hirota, M. Kubo, W. McArdle, A. J. Henderson, J. P. Kemp, J. Zheng, G. D. Smith, F. Rüschendorf, A. Bauerfeind, M. A. Lee-Kirsch, A. Arnold, G. Homuth, C. O. Schmidt, E. Mangold, S. Cichon, T. Keil, E. Rodríguez, A. Peters, A. Franke, W. Lieb, N. Novak, R. Fölster-Holst, M. Horikoshi, J. Pekkanen, S. Sebert, L. L. Husemoen, N. Grarup, J. C. de Jongste, F. Rivadeneira, A. Hofman, V. W. Jaddoe, S. G. Pasmans, N. J. Elbert, A. G. Uitterlinden, G. B. Marks, P. J. Thompson, M. C. Matheson, C. F. Robertson, Australian Asthma Genetics Consortium (AAGC), J. S. Ried, J. Li, X. B. Zuo, X. D. Zheng, X. Y. Yin, L. D. Sun, M. McAleer, G. M. O'Regan, C. M. Fahy, L. E. Campbell, M. Macek, M. Kurek, D. Hu, C. Eng, D. S. Postma, B. Feenstra, F. Geller, J. J. Hottenga, C. M. Middeldorp, P. Hysi, V. Bataille, T. Spector, C. M. Tiesler, E. Thiering, B. Pahukasahasram, J. J. Yang, M. Imboden, S. Huntsman, N. Vilor-Tejedor, C. L. Relton, R. Myhre, W. Nystad, A. Custovic, S. T. Weiss, D. A. Meyers, C. Söderhäll, E. Melén, C. Ober, B. A. Raby, A. Simpson, B. Jacobsson, J. W. Holloway, H. Bisgaard, J. Sunyer, N. M. P. Hensch, L. K. Williams, K. M. Godfrey, C. A. Wang, D. I. Boomsma, M. Melbye, G. H. Koppelman, D. Jarvis, W. McLean, A. D. Irvine, X. J. Zhang, H. Hakonarson, C. Gieger, E. G. Burchard, N. G. Martin, L. Duijts, A. Linneberg, M. R. Jarvelin, M. M. Noethen, S. Lau, N. Hübner, Y. A. Lee, M. Tamari, D. A. Hinds, D. Glass, S. J. Brown, J. Heinrich, D. M. Evans, S. Weidinger, Multi-ancestry genome-wide association study of 21,000 cases and 95,000 controls identifies new risk loci for atopic dermatitis. *Nat. Genet.* **47**, 1449–1456 (2015).
55. A. Mahajan, J. Wessel, S. M. Willems, W. Zhao, N. R. Robertson, A. Y. Chu, W. Gan, H. Kitajima, D. Taliun, N. W. Rayner, X. Guo, Y. Lu, M. Li, R. A. Jensen, Y. Hu, S. Huo, K. K. Lohman, W. Zhang, J. P. Cook, B. P. Prins, J. Flannick, N. Grarup, V. V. Trubetskoy, J. Kravic, Y. J. Kim, D. V. Rybin, H. Yaghootkar, M. Müller-Nurasyid, K. Meidtner, R. Li-Gao, T. V. Varga, J. Marten, J. Li, A. V. Smith, P. An, S. Ligthart, S. Gustafsson, G. Malerba, A. Demirkan, J. F. Tajes, V. Steinthorsdottir, M. Wuttke, C. Lecoeur, M. Preuss, L. F. Bielak, M. Graff, H. M. Highland, A. E. Justice, D. J. Liu, E. Marouli, G. M. Peloso, H. R. Warren, ExomeBP Consortium, MAGIC Consortium, GIANT Consortium, S. Afaq, S. Afzal, E. Ahlqvist, P. Almgren, N. Amin, L. B. Bang, A. G. Bertoni, C. Bombieri, J. Bork-Jensen, I. Brandslund, J. A. Brody, N. P. Burtt, M. Canouil, Y. D. I. Chen, Y. S. Cho, C. Christensen, S. V. Eastwood, K. U. Eckardt, K. Fischer, G. Gambaro, V. Giedraitis, M. L. Grove, H. G. de Haan, S. Hackinger, Y. Hai, S. Han, A. Tybjærg-Hansen, M. F. Hivert, B. Isomaa, S. Jäger, M. E. Jørgensen, T. Jørgensen, A. Käräjämäki, B. J. Kim, S. S. Kim, H. A. Koistinen, P. Kovacs, J. Kriebel, F. Kronenberg, K. Läll, L. A. Lange, J. J. Lee, B. Lehne, H. Li, K. H. Lin, A. Linneberg, C. T. Liu, J. Liu, M. Loh, R. Mägi, V. Mamakou, R. McKean-Cowdin, G. Nadkarni, M. Neville, S. F. Nielsen, I. Ntalla, P. A. Peyser, W. Rathmann, K. Rice, S. S. Rich, L. Rode, O. Rolandsson, S. Schönherr, E. Selvin, K. S. Small, A. Stančáková, P. Surendran, K. D. Taylor, T. M. Teslovich, B. Thorand, G. Thorleifsson, A. Tin, A. Tönjes, A. Varbo, D. R. Witte, A. R. Wood, P. Yajnik, J. Yao, L. Yengo, R. Young, P. Amouyel, H. Boeing, E. Boerwinkle, E. P. Bottinger, R. Chowdhury, F. S. Collins, G. Dedoussis, A. Dehghan, P. Deloukas, M. M. Ferrario, J. Ferrières, J. C. Florez, P. Frossard, V. Gudnason, T. B. Harris, S. R. Heckbert, J. M. M. Howson, M. Ingelsson, S. Kathiresan, F. Kee, J. Kuusisto, C. Langenberg, L. J. Launer, C. M. Lindgren, S. Männistö, T. Meitinger, O. Melander, K. L. Mohlke, M. Moitry, A. D. Morris, A. D. Murray, R. de Mutsert, M. Orho-Melander, K. R. Owen, M. Perola, A. Peters, M. A. Province, A. Rasheed, P. M. Ridker, F. Rivadineira, F. R. Rosendaal, A. H. Rosengren, V. Salomaa, W. H. H. Sheu, R. Sladek, B. H. Smith, K. Strauch, A. G. Uitterlinden, R. Varma, C. J. Willer, M. Blüher, A. S. Butterworth, J. C. Chambers, D. I. Chasman, J. Danesh, C. van Duijn, J. Dupuis, O. H. Franco, P. W. Franks, P. Froguel, H. Grallert, L. Groop, B. G. Han, T. Hansen, A. T. Hattersley, C. Hayward, E. Ingelsson, S. L. R. Kardia, F. Karpe, J. S. Kooner, A. Köttgen, K. Kuulasmaa, M. Laakso, X. Lin, L. Lind, Y. Liu, R. J. F. Loos, J. Marchini, A. Metspalu, D. Mook-Kanamori, B. G. Nordestgaard, C. N. A. Palmer, J. S. Pankow, O. Pedersen, B. M. Psaty, R. Rauramaa, N. Sattar, M. B. Schulze, N. Soranzo, T. D. Spector, K. Stefansson, M. Stumvoll, U. Thorsteinsdottir, T. Tuomi, J. Tuomilehto, N. J. Wareham, J. G. Wilson, E. Zeggini, R. A. Scott, I. Barroso, T. M. Frayling, M. O. Goodarzi, J. B. Meigs, M. Boehnke, D. Saleheen, A. P. Morris, J. I. Rotter, M. I. McCarthy, Refining the accuracy of validated target identification through coding variant fine-mapping in type 2 diabetes. *Nat. Genet.* **50**, 559–571 (2018).
56. I. E. Jansen, J. E. Savage, K. Watanabe, J. Bryois, D. M. Williams, S. Steinberg, J. Sealock, I. K. Karlsson, S. Hägg, L. Athanasiu, N. Voyle, P. Proitsi, A. Witoelar, S. Stringer, D. Aarsland, I. S. Almdahl, F. Andersen, S. Bergh, F. Bettella, S. Bjornsson, A. Brækhus, G. Bråthen, C. de Leeuw, R. S. Desikan, S. Djurovic, L. Dumitrescu, T. Fladby, T. J. Hohman, P. V. Jonsson, S. J. Kiddle, A. Rongve, I. Saltvedt, S. B. Sando, G. Selbæk, M. Shoai, N. G. Skene, J. Snaedal, E. Stordal, I. D. Ulstein, Y. Wang, L. R. White, J. Hardy, J. Hjerling-Leffler, P. F. Sullivan, W. M. van der Flier, R. Dobson, L. K. Davis, H. Stefansson, K. Stefansson, N. L. Pedersen, S. Ripke, O. A. Andreassen, D. Posthuma, Genome-wide meta-analysis identifies new loci and functional pathways influencing Alzheimer's disease risk. *Nat. Genet.* **51**, 404–413 (2019).
57. L. Jiang, Z. Zheng, H. Fang, J. Yang, A generalized linear mixed model association tool for biobank-scale data. *Nat. Genet.* **53**, 1616–1621 (2021).
58. C. P. Nelson, A. Goel, A. S. Butterworth, S. Kanoni, T. R. Webb, E. Marouli, L. Zeng, I. Ntalla, F. Y. Lai, J. C. Hopewell, O. Giannakopoulou, T. Jiang, S. E. Hamby, E. D. Angelantonio, T. L. Assimes, E. P. Bottinger, J. C. Chambers, R. Clarke, C. N. A. Palmer, R. M. Cubbon, P. Ellinor, R. Ermel, E. Evangelou, P. W. Franks, C. Grace, D. Gu, A. D. Hingorani, J. M. M. Howson, E. Ingelsson, A. Kastrati, T. Kessler, T. Kyriakou, T. Lehtimäki, X. Lu, Y. Lu, W. März, R. M. Pherson, A. Metspalu, M. Pujades-Rodriguez, A. Ruusalepp, E. E. Schadt, A. F. Schmidt, M. J. Sweeting, P. A. Zalloua, K. A. Ghalayini, B. D. Keavney, J. S. Kooner, R. J. F. Loos, R. S. Patel, M. K. Rutter, M. Tomaszewski, I. Tzoulaki, E. Zeggini, J. Erdmann, G. Dedoussis, J. L. M. Björkegren, EPIC-CVD Consortium, CARDIoGRAMplusC4D, UK Biobank CardioMetabolic Consortium CHD working group, H. Schunkert, M. Farrall, J. Danesh, N. J. Samani, H. Watkins, P. Deloukas, Association analyses based on false discovery rate implicate new loci for coronary artery disease. *Nat. Genet.* **49**, 1385–1391 (2017).
59. E. M. Pedersen, E. Agerbo, O. Plana-Ripoll, J. Steinbach, M. D. Krebs, D. M. Hougaard, T. Werge, M. Nordentoft, A. D. Børglum, K. L. Musliner, A. Ganna, A. J. Schork, P. B. Mortensen, J. J. McGrath, F. Privé, B. J. VilhjáImsson, ADuLT: An efficient and robust time-to-event GWAS. *Nat. Commun.* **14**, 5553 (2023).
60. E. Sollis, A. Mosaku, A. Abid, A. Buniello, M. Cerezo, L. Gil, T. Groza, O. Güneş, P. Hall, J. Hayhurst, A. Ibrahim, Y. Ji, S. John, E. Lewis, J. A. L. MacArthur, A. McMahon, D. Osumi-Sutherland, K. Panoutsopoulou, Z. Pendlington, S. Ramachandran, R. Stefancsik, J. Stewart, P. Whetzel, R. Wilson, L. Hindorff, F. Cunningham, S. A. Lambert, M. Inouye, H. Parkinson, L. W. Harris, The NHGRI-EBI GWAS Catalog: Knowledgebase and deposition resource. *Nucleic Acids Res.* **51**, D977–D985 (2023).
61. G. Yu, L. G. Wang, Q. Y. He, ChIPseeker: An R/Bioconductor package for ChIP peak annotation, comparison and visualization. *Bioinformatics* **31**, 2382–2383 (2015).
62. R. Browaeys, W. Saelens, Y. Saeys, NicheNet: Modeling intercellular communication by linking ligands to target genes. *Nat. Methods* **17**, 159–162 (2020).

Acknowledgments: We are grateful to the organ donors and donors' families, whose gifts made this research and future discoveries possible. We also acknowledge the invaluable efforts of the HPAP consortium and the Network for Pancreatic Organ Donors with Diabetes (nPOD; www.jdrfnpod.org/) in facilitating the recovery and distribution of donor organs used in this study. We thank S. Shapira and the PANC-DB team—N. Samanta, D. Hu, and N. Burget—for dedicated support. We further appreciate the insightful discussions with M. Betts, E. T. Luning Prak, A. Powers, T. Brusko, and M. Atkinson, as well as the members of the Vahedi and Faryabi laboratories for valuable input and collaboration.
Funding: This study was supported by NIH U01DK112217 and U01DK123594 (to A.N., K.H.K., G.V., and R.B.F.); NIH R01DK133453 and Breakthrough T1D CDA-2020-946-S-B (M.S.); NIH R01CA248041 and CA-230800 (to R.B.F.); the Burroughs Welcome Fund; the Chan Zuckerberg Initiative Award; and NIH R01AI168240, R01AI168136, U01DK127768, U01DA052715 (G.V.). **Author contributions:** Conceptualization: M.A., P.R., Y.Z., R.B.F., and G.V. Resources: C.L. and A.N. procured human pancreatic tissues. M.A., S.R., I.J., and A.C. processed human organ tissues; M.Y. and S.R. harvested mouse organ tissues; and S.R. and M.A. processed the mouse tissues. V.L. and M.S. provided NOD mice and helped with insulitis experiments. Methodology: M.A. performed multiome single-cell experiments with help from Y.Z. and A.C. M.F. performed the original single-cell experiments in NOD mice. Software: P.R. performed computational analysis related to multiome data in humans. M.A. performed computational analysis related to multiome data in mice and genetics analysis. A.J. performed IF image analysis. Validation: W.W., Z.M., Y.L., and M.Y. performed IF experiments. Writing: original draft: M.A. Writing: G.V. wrote the manuscript

with feedback from all coauthors. Funding acquisition: G.V., R.B.F., A.N., and K.H.K. acquired funding. Supervision: R.B.F. and G.V. **Competing interests:** The authors declare that they have no competing interests. **Data and materials availability:** The raw sequencing data in this manuscript have been deposited in the NCBI GEO database under accession number GSE269540 and Panc-DB (https://hpap.pmacs.upenn.edu/). The analysis code used in this study is publicly available on GitHub (https://github.com/VahediLab/Human_Mouse_T1D_Multiome) and has been archived on Zenodo (*43*). All other data needed to evaluate the conclusions in the paper are present in the paper and/or the Supplementary Materials.

Submitted 15 May 2025
Accepted 14 October 2025
Published 21 November 2025
10.1126/sciimmunol.adz0472